

This item is likely protected under Title 17 of the U.S. Copyright Law. Unless on a Creative Commons license, for uses protected by Copyright Law, contact the copyright holder or the author.

Access to this work was provided by the University of Maryland, Baltimore County (UMBC) ScholarWorks@UMBC digital repository on the Maryland Shared Open Access (MD-SOAR) platform.

Please provide feedback

Please support the ScholarWorks@UMBC repository by emailing scholarworks-group@umbc.edu and telling us what having access to this work means to you and why it's important to you. Thank you.



The Steady Global Corona and Solar Wind: A Three-dimensional MHD Simulation with Turbulence Transport and Heating

Arcadi V. Usmanov^{1,2} , William H. Matthaeus¹ , Melvyn L. Goldstein³ , and Rohit Chhiber¹

¹ Department of Physics and Astronomy, University of Delaware, Newark, DE 19716, USA; usmanov@udel.edu

² NASA Goddard Space Flight Center, Greenbelt, MD 20771, USA

³ University of Maryland Baltimore County, Baltimore, MD 21250, USA

Received 2018 June 8; revised 2018 July 24; accepted 2018 July 25; published 2018 September 18

Abstract

We present a fully three-dimensional magnetohydrodynamic model of the solar corona and solar wind with turbulence transport and heating. The model is based on Reynolds-averaged solar wind equations coupled with transport equations for turbulence energy, cross helicity, and correlation scale. The model includes separate energy equations for protons and electrons and accounts for the effects of electron heat conduction, radiative cooling, Coulomb collisions, Reynolds stresses, eddy viscosity, and turbulent heating of protons and electrons. The computational domain extends from the coronal base to 5 au and is divided into two regions: the inner (coronal) region, 1–30 R_{\odot} , and the outer (solar wind) region, 30 R_{\odot} –5 au. Numerical steady-state solutions in both regions are constructed by time relaxation in the frame of reference corotating with the Sun. Inner boundary conditions are specified using either a tilted-dipole approximation or synoptic solar magnetograms. The strength of solar dipole is adjusted, and a scaling factor for magnetograms is estimated by comparison with *Ulysses* observations. Except for electron temperature, the model shows reasonable agreement with *Ulysses* data during its first and third fast latitude transits. We also derive a formula for the loss of angular momentum caused by the outflowing plasma. The formula takes into account the effects of turbulence. The simulation results show that turbulence can notably affect the Sun’s loss of angular momentum.

Key words: magnetohydrodynamics (MHD) – methods: numerical – solar wind – Sun: corona – Sun: rotation – turbulence

1. Introduction

The Sun’s magnetic field is generated in the solar convective zone by a dynamo mechanism. The magnetic field emerges from the solar surface to be pulled into interplanetary space by the expanding coronal plasma, the solar wind. Close to the Sun, the magnetic energy strongly exceeds other forms of energy, including the kinetic and thermal energies of the coronal plasma. As a result, the global structure of the corona and solar wind is largely determined by the distribution of magnetic field on the solar photosphere. The magnetic field weakens rapidly with distance, and the initially subsonic and sub-Alfvénic solar wind accelerates to become both supersonic and super-Alfvénic beyond heliocentric distances ~ 5 – $15 R_{\odot}$, where R_{\odot} is the solar radius. The kinetic energy then takes the lead and dominates the thermal and magnetic energies in the subsequent evolution of the solar wind plasma out to the heliospheric termination shock.

The complex structure of the solar wind arises, in part, from the inhomogeneity of photospheric magnetic field, as well as a consequence of solar rotation, which leads to the formation of corotating interaction regions (CIRs; Hundhausen 1972; Gosling & Pizzo 1999). Even under stationary solar conditions, solar rotation causes streams to become radially aligned and, therefore, to interact, which produces compressions (as fast streams overtake slow ones) and rarefactions (as slow streams trail fast ones). The forward and reverse pressure waves bounding the CIRs often evolve into forward and reverse shock pairs beyond 2 au (Gosling & Pizzo 1999). The CIRs are associated with a specific pattern of nonradial flows that tend to relieve compressions and fill rarefactions (Pizzo 1978, 1982). This highly complex and inhomogeneous structure can be described realistically only within a fully three-dimensional model.

The problem of self-consistent three-dimensional magnetohydrodynamic (MHD) simulation of the solar corona and solar wind is highly challenging. Consequently, a number of simplifying assumptions have been commonly employed starting from the pioneering studies of Pneuman & Kopp (1971) and Endler (1971). Aside from reducing the dimensionality of the problem, the most popular approach is to exclude the subsonic/sub-Alfvénic flow region completely by moving the inner boundary outward into the supersonic and super-Alfvénic flow regime, typically to distances of $\sim 20 R_{\odot}$. The expediency of eliminating the most computationally expensive transonic/trans-Alfvénic region is evident, but it is strongly offset by the need to translate the measured magnetic fields from the photospheric level to the distant boundary and to specify all other flow quantities on the boundary. The potential field source-surface (PFSS) model (Altschuler & Newkirk 1969; Schatten et al. 1969; Wang & Sheeley 1992) and the Wang–Sheeley–Arge empirical relation between solar wind speed and the coronal field expansion factor (Levine et al. 1977; Wang & Sheeley 1990, 1997; Arge et al. 2003) are routinely used for prescribing magnetic field and flow parameters on the boundary (e.g., Odstrčil 2003; Detman et al. 2006, 2011; Wiengarten et al. 2013; Shiota et al. 2014; Merkin et al. 2016). While such an approach simplifies the problem significantly, it is physically deficient. The issue is that a Parker-type (transonic) solution is a singular solution that passes through a critical point at which the flow speed equals the speed of sound (Parker 1958). This condition implies a certain relation between flow parameters that should be satisfied on the boundary (Steinolfson & Nakagawa 1976). However, if the inner boundary is placed outside the critical point and all flow parameters are set independently on the boundary, the relation is in general not satisfied, and any solution traced back to the coronal base is not necessarily a transonic (i.e.,

critical) solution. Thus, to construct physically meaningful transonic solutions, it is mandatory to place the inner boundary near the coronal base in the subsonic/sub-Alfvénic flow regime.

In addition to the requirements that the solutions both start from the coronal base and be three-dimensional, coronal models should include additional extended sources of momentum and energy to be able to reproduce the properties of fast solar wind (Munro & Jackson 1977; Barnes et al. 1995; Usmanov et al. 2000; Usmanov & Goldstein 2003). The sources are often described by ad hoc formulae (e.g., Hartle & Barnes 1970; Wang et al. 1998; Groth et al. 2000; Nakamizo et al. 2009; Feng et al. 2010, 2014; Yalim et al. 2017). However, as the physical mechanism of the extended heating and acceleration is generally believed to be a flux of low-frequency Alfvén waves generated in the magnetic carpet and propagating away from the Sun along the magnetic field, it is natural to reformulate the governing equations by including an evolution equation for Alfvén waves and wave effects in the momentum and energy equations. The waves propagating outward in a spherically expanding geometry exert a ponderomotive force (an outward wave pressure gradient) that accelerates the flow (e.g., Belcher 1971; Hollweg 1990). Interaction of the waves with those reflected from density and magnetic field gradients (and thus propagating inward) can generate turbulence that, in turn, leads to turbulent heating (Matthaeus et al. 1999a; Dmitruk et al. 2002).

There exist only a handful of fully three-dimensional solar wind models that start from the coronal base and extend at least to 1 au, which enables their output to be directly compared with spacecraft observations (Usmanov 1993a, 1993b, 1996; Groth et al. 2000; Riley et al. 2001, 2012; Hayashi 2005; Tóth et al. 2005; Feng et al. 2010, 2014; van der Holst et al. 2014). The first model of this type by Usmanov (1993a, 1993b) was a generalization of streamer simulation studies (Steinolfson et al. 1982; Linker et al. 1990), combined with supersonic/super-Alfvénic steady-state flow calculations (Pizzo 1978, 1982). That model was also the first to implement synoptic solar magnetograms as boundary conditions for global solar wind simulations and to produce a fully three-dimensional time-dependent simulation of a series of coronal mass ejections propagating from the coronal base to 1.5 au, which enabled comparison with Earth-orbiting spacecraft observations (Usmanov & Dryer 1995). Using the short-wavelength Wentzel–Kramers–Brillouin (WKB) approximation, Usmanov (1996) included a flux of Alfvén waves propagating away from the Sun that provided additional acceleration and heating of the solar wind. The three-dimensional solar wind equations have also been augmented to include an evolution equation for Alfvén wave energy density as discussed by Dewar (1970), Bretherton (1971), and Jacques (1978).

The WKB approach was extensively explored with one-dimensional solar wind models (e.g., Belcher 1971; Hollweg 1978; Jacques 1978; Esser et al. 1986; Wang 1993; Habbal et al. 1994; Chandran et al. 2011) that proved that waves could provide the additional acceleration required to reproduce fast solar wind. WKB wave acceleration was also incorporated into solar wind models by Usmanov et al. (2000) and Usmanov & Goldstein (2003). Those models agreed with the Wang–Sheeley empirical relation and produced a bimodal solar wind consistent with *Ulysses* observations (Usmanov & Goldstein 2003). More recently, the WKB wave-driven approach was employed in two- and three-dimensional solar wind models by Chen & Hu (2001), Hu et al. (2003), Li et al. (2004),

Sokolov et al. (2013), and van der Holst et al. (2010, 2014). Although the wave-driven models produce useful results, the physics contained in those models is limited. In particular, there are no nonlinear interactions between the fluctuations, and hence no turbulence or self-consistent turbulent heating. Furthermore, the assumption of equipartition of kinetic and magnetic fluctuation energy is at odds with observations (Matthaeus & Goldstein 1982; Matthaeus & Velli 2011).

Another approach to modeling wave effects in the solar wind is based on turbulence transport models that include effects of the cascade and dissipation of turbulence (e.g., Matthaeus et al. 1994, 1999b; Dmitruk et al. 2001; Smith et al. 2001; Isenberg et al. 2003; Matthaeus et al. 2004; Breech et al. 2008; Verdini et al. 2010; Cranmer & van Ballegoijen 2012; Zank et al. 2012, 2017; Lionello et al. 2014a, 2014b). As implemented in the references cited, the models are one-dimensional, the geometry of the magnetic/flow tubes is predefined, and the effects of shear driving are introduced only in an ad hoc manner. Recently, Usmanov et al. (2009, 2011, 2012, 2014, 2016; see also Kryukov et al. 2012; Wiengarten et al. 2015, 2016; Shiota et al. 2017) have bridged the gap between large-scale solar wind and turbulence transport models by developing three-dimensional solar wind models where the mean-flow solar wind and turbulence transport equations are solved simultaneously. The large-scale flow structure and the magnetic geometry have been computed including the influence of turbulence (except for Shiota et al. 2017), while the turbulence properties are dependent on the large-scale flow and magnetic field.

The plasma, magnetic field, and turbulence parameters computed with the Usmanov et al. (2014) model have been used to calculate nondimensional collisional age, which represents the number of collisional timescales that have elapsed over the travel time of a solar wind parcel (Chhiber et al. 2016). Chhiber et al. (2017) computed the cosmic-ray diffusion coefficients for scattering off of the magnetic turbulence throughout the inner heliosphere from 2 R_{\odot} to 3 au. The results from Usmanov et al. (2014) were also used to study early stages in the development of turbulence in the young solar wind based on the computed locations of the Alfvén and plasma beta equals unity surfaces (Chhiber et al. 2018a).

A significant limitation of the Usmanov et al. (2014) model is that the turbulence transport equations are written under the assumption that the Alfvén speed is much smaller than the flow speed and, as a result, the turbulence transport model is implemented only in the region beyond 0.3 au. Meanwhile, a simpler (WKB) model (Usmanov et al. 2000; Usmanov & Goldstein 2003) is used inside 0.3 au. The goal of the present paper is to generalize the turbulence transport model by relaxing the assumption that the flow is highly super-Alfvénic and to implement the generalized transport model both in the coronal region inside 30 R_{\odot} and in the solar wind region up to 5 au. Doing this produces a more unified, widely applicable and physically complete model to study a sequence of problems that are of great current interest, especially in the context of the forthcoming *Parker Solar Probe* era. In the following section, we describe in detail the model formulation and discuss the initial and boundary conditions. The results of the simulation and comparison with *Ulysses* data are presented in Section 3, where we also examine several detailed features of the solutions. We conclude with a summary of the results and a discussion of limitations and future extensions of the model in Section 4.

2. Mathematical Formulation

2.1. Governing Equations in the Rotating Frame

Following Usmanov et al. (2014) and neglecting effects of pickup protons (as we do not include the distant solar wind beyond 5 au in this study), we consider the following MHD equations in the frame of reference corotating with the Sun:

$$\frac{\partial \rho}{\partial t} + \nabla \cdot (\rho \mathbf{v}) = 0, \quad (1)$$

$$\frac{\partial \mathbf{v}}{\partial t} + (\mathbf{v} \cdot \nabla) \mathbf{v} + \frac{1}{\rho} \nabla (P_S + P_E) - \frac{(\nabla \times \mathbf{B}) \times \mathbf{B}}{4\pi\rho} + \frac{GM_\odot}{r^2} \hat{\mathbf{r}} + 2\boldsymbol{\Omega} \times \mathbf{v} + \boldsymbol{\Omega} \times (\boldsymbol{\Omega} \times \mathbf{r}) = 0, \quad (2)$$

$$\frac{\partial \mathbf{B}}{\partial t} = \nabla \times (\mathbf{v} \times \mathbf{B}), \quad (3)$$

$$\begin{aligned} \frac{\partial P_S}{\partial t} + (\mathbf{v} \cdot \nabla) P_S + \gamma P_S \nabla \cdot \mathbf{v} \\ = (\gamma - 1) \left(f_p Q_T + \frac{P_E - P_S}{\tau_{SE}} \right), \end{aligned} \quad (4)$$

$$\begin{aligned} \frac{\partial P_E}{\partial t} + (\mathbf{v} \cdot \nabla) P_E + \gamma P_E \nabla \cdot \mathbf{v} = (\gamma - 1) [(1 - f_p) Q_T \\ + \frac{P_S - P_E}{\tau_{SE}} - \nabla \cdot \mathbf{q}_E - Q_{\text{rad}}]. \end{aligned} \quad (5)$$

In the above equations, the independent variables are time t and the heliocentric position vector \mathbf{r} . The dependent variables ρ , \mathbf{v} , \mathbf{B} , P_S , and P_E represent mass density, velocity in the frame rotating with the Sun, magnetic field, and proton and electron thermal pressure, respectively. We assume that both protons and electrons move with the same velocity \mathbf{v} , although they can have different temperatures. We neglect the mass of electron m_e in comparison with the proton mass m_p , so the mass density $\rho \approx N_S m_p$, where N_S is the number density of protons. Other notations are the electron heat flux \mathbf{q}_E , the timescale of Coulomb collisions between protons and electrons τ_{SE} , the solar mass M_\odot , the solar angular velocity vector $\boldsymbol{\Omega}$, the adiabatic index γ , the universal gravitational constant G , and a unit vector in the radial direction $\hat{\mathbf{r}}$. An additional heating source per unit mass due to turbulence dissipation Q_T is assumed to be split between protons and electrons according to the factor f_p . Q_{rad} is the radiative cooling rate. For a fully ionized and optically thin plasma $Q_{\text{rad}} = N_E^2 \Phi(T_E)$, where T_E is the electron temperature, $N_E = N_S$ is the number density of electrons, and $\Phi(T_E)$ is a tabulated radiation loss function of electron temperature (e.g., Priest 1982).

The equipartition timescale due to Coulomb collisions between protons and electrons τ_{SE} can be written as (Spitzer 1962; Hartle & Sturrock 1968)

$$\tau_{SE} = \frac{3m_p (k_B T_E)^{3/2}}{8(2\pi m_e)^{1/2} e^4 N_E \ln \Lambda}, \quad (6)$$

where

$$\ln \Lambda = \ln \left[\frac{3(k_B T_E)^{3/2}}{2\pi^{1/2} e^3 N_E^{1/2}} \right] \quad (7)$$

is the Coulomb logarithm, e is the elementary charge, and k_B is the Boltzmann constant.

By splitting the magnetic field vector into potential and nonpotential parts (Tanaka 1994; Powell et al. 1999) $\mathbf{B} = \mathbf{B}_0 + \mathbf{B}_1$, where \mathbf{B}_0 is an intrinsic potential field that satisfies the conditions $\partial \mathbf{B}_0 / \partial t = 0$ and $\nabla \times \mathbf{B}_0 = 0$, and using the mass conservation Equation (1), we can rewrite the momentum Equation (2) in a conservative form as

$$\begin{aligned} \frac{\partial(\rho \mathbf{v})}{\partial t} + \nabla \cdot \left\{ \rho \mathbf{v} \mathbf{v} + \left[P_S + P_E + \frac{B_1^2}{8\pi} + \frac{(\mathbf{B}_0 \cdot \mathbf{B}_1)}{4\pi} \right] \mathbf{I} \right. \\ \left. - \frac{\mathbf{B}_1 \mathbf{B}_1 + \mathbf{B}_1 \mathbf{B}_0 + \mathbf{B}_0 \mathbf{B}_1}{4\pi} \right\} = - \frac{\rho G M_\odot}{r^2} \hat{\mathbf{r}} \\ - \rho [2\boldsymbol{\Omega} \times \mathbf{v} + \boldsymbol{\Omega} \times (\boldsymbol{\Omega} \times \mathbf{r})], \end{aligned} \quad (8)$$

where \mathbf{I} is the unit matrix. The decomposition of magnetic field into potential and nonpotential parts and solving for the deviation from the potential field significantly reduce numerical errors in computing the Lorentz force. This is critically important especially close to the Sun, where the magnetic field is dominant and nearly potential. The induction Equation (3) then takes the form

$$\frac{\partial \mathbf{B}_1}{\partial t} = \nabla \times (\mathbf{v} \times \mathbf{B}). \quad (9)$$

2.2. Reynolds-averaged Mean-flow Equations

After decomposing the dependent variables into mean and fluctuating parts (for details see Usmanov et al. 2014), we apply the Reynolds ensemble averaging to Equations (1)–(4), (5), (8), and (9). Retaining the same notation for dependent variables that now represent ensemble averages, we can cast Equations (8)–(9) as

$$\begin{aligned} \frac{\partial(\rho \mathbf{u})}{\partial t} + \nabla \cdot \left\{ \rho \mathbf{v} \mathbf{u} + \left[P_S + P_E + \frac{\langle B'^2 \rangle}{8\pi} + \frac{B_1^2}{8\pi} \right. \right. \\ \left. \left. + \frac{(\mathbf{B}_0 \cdot \mathbf{B}_1)}{4\pi} \right] \mathbf{I} - \frac{\mathbf{B}_1 \mathbf{B}_1 + \mathbf{B}_1 \mathbf{B}_0 + \mathbf{B}_0 \mathbf{B}_1}{4\pi} + \mathcal{R} \right\} \\ + \rho \left(\frac{GM_\odot}{r^2} \hat{\mathbf{r}} + \boldsymbol{\Omega} \times \mathbf{u} \right) = 0, \end{aligned} \quad (10)$$

$$\frac{\partial \mathbf{B}_1}{\partial t} = \nabla \times (\mathbf{v} \times \mathbf{B} + \varepsilon_m \sqrt{4\pi\rho}), \quad (11)$$

where

$$\mathcal{R} = \left\langle \rho \mathbf{v}' \mathbf{v}' - \frac{1}{4\pi} \mathbf{B}' \mathbf{B}' \right\rangle \quad (12)$$

is the Reynolds stress tensor, $\varepsilon_m = \langle \mathbf{v}' \times \mathbf{B}' \rangle (4\pi\rho)^{-1/2}$ is the mean turbulent electric field, \mathbf{v}' and \mathbf{B}' are the fluctuating components of velocity and magnetic field, respectively, $\langle \dots \rangle$ is the ensemble averaging operator, $\mathbf{u} = \mathbf{v} + \mathbf{w}$ is the velocity in the inertial frame, and $\mathbf{w} = \boldsymbol{\Omega} \times \mathbf{r}$.

In deriving Equation (10) we used the relation

$$\begin{aligned} - \mathbf{w} \frac{\partial \rho}{\partial t} - \nabla \cdot (\rho \mathbf{v} \mathbf{w}) + \rho [2\boldsymbol{\Omega} \times \mathbf{v} + \boldsymbol{\Omega} \times (\boldsymbol{\Omega} \times \mathbf{r})] \\ = \rho \boldsymbol{\Omega} \times \mathbf{u}, \end{aligned} \quad (13)$$

which can be verified using the mass conservation Equation (1) and the vector identity $(\mathbf{A} \cdot \nabla)(\boldsymbol{\Omega} \times \mathbf{r}) = \boldsymbol{\Omega} \times \mathbf{A}$, where \mathbf{A} is any vector. Also, it is easy to show that $\nabla \cdot \mathbf{w} = 0$ and therefore $\nabla \cdot \mathbf{v} = \nabla \cdot \mathbf{u}$. We emphasize that even though the time derivative on the left-hand side of the momentum

Equation (10) contains the velocity in the inertial frame \mathbf{u} , the equation is written in the frame of reference rotating with the angular velocity $\boldsymbol{\Omega}$. A similar form of the momentum equation was used, e.g., by Agarwal & Deese (1987).

An assumption underlying the derivation of Reynolds-averaged equations in our case is that the turbulence is locally incompressible, i.e., the fluctuations of density and thermal pressures can be neglected (Usmanov et al. 2009, 2011, 2012, 2014, 2016). As a result, the continuity Equation (1) and the pressure Equations (4)–(5) retain their form after applying the Reynolds decomposition and averaging.

2.3. Electron Heat Flux

In the solar corona and solar wind, the heat flux is carried primarily by electrons, while the proton heat flux is negligible (e.g., Cranmer et al. 2009). The electron heat flux is directed essentially along the magnetic field. Close to the Sun ($r \lesssim 5 R_\odot$), where the coronal plasma is relatively dense and collisions between electrons are relatively frequent, the electron heat flux can be described by the classical “collisional” approximation (Spitzer 1962)

$$\mathbf{q}_S = -\kappa \hat{\mathbf{B}}(\hat{\mathbf{B}} \cdot \nabla) T_E, \quad (14)$$

where

$$\kappa = 20\epsilon\delta_T \left(\frac{2}{\pi}\right)^{3/2} \frac{k_B(k_B T_E)^{5/2}}{m_e^{1/2} e^4 \ln \Lambda},$$

$\epsilon = 0.419$, and $\delta_T = 0.225$. Beyond a few solar radii, the coronal plasma is essentially collisionless and the heat is transported by the suprathermal tail of the electron distribution (Scudder & Olbert 1979). To describe the heat flux in this case, Hollweg (1974, 1976) proposed a so-called “collisionless” model

$$\mathbf{q}_H = \frac{3}{2} \alpha_H P_E \mathbf{v}, \quad (15)$$

where α_H is a parameter of order unity. Note that the velocity in Equation (15) is the velocity in the rotating frame \mathbf{v} . Since in steady state \mathbf{v} is parallel to \mathbf{B} (Pizzo 1982), the electron heat flux (15) is directed along the magnetic field.

Cranmer et al. (2009) have shown that Hollweg’s expression (15) reproduces *Helios* and *Ulysses* observations for the average $\alpha_H = 1.05$. Following Chandran et al. (2011; see also van der Holst et al. 2014), we specify the electron heat flux by interpolating between the two regimes described by Equations (14) and (15),

$$\mathbf{q}_E = \psi \mathbf{q}_H + (1 - \psi) \mathbf{q}_S, \quad (16)$$

where

$$\psi = \frac{(r/r_H)^2}{1 + (r/r_H)^2}, \quad (17)$$

and r_H is a free parameter of order $5 R_\odot$.

2.4. Turbulence Transport Equations

Our model includes the turbulence transport equations derived by Usmanov et al. (2014). Assuming that the velocity and magnetic field fluctuations are transverse to the mean magnetic field \mathbf{B} and neglecting effects of pickup protons, the transport Equations (A3), (A4), and (18) in Usmanov et al. (2014) can be

written as

$$\begin{aligned} \frac{\partial Z^2}{\partial t} = & -(\mathbf{v} \cdot \nabla) Z^2 - \frac{Z^2(1 - \sigma_D)}{2} \nabla \cdot \mathbf{u} - \frac{2}{\rho} \mathcal{R} : \nabla \mathbf{u} \\ & - 2\epsilon_m \cdot (\nabla \times \mathbf{V}_A) + (\mathbf{V}_A \cdot \nabla)(Z^2 \sigma_c) \\ & - Z^2 \sigma_c \nabla \cdot \mathbf{V}_A - \frac{\alpha f^+(\sigma_c) Z^3}{\lambda}, \end{aligned} \quad (18)$$

$$\begin{aligned} \frac{\partial(Z^2 \sigma_c)}{\partial t} = & -(\mathbf{v} \cdot \nabla)(Z^2 \sigma_c) - \frac{Z^2 \sigma_c}{2} \nabla \cdot \mathbf{u} - \frac{2}{\rho} \mathcal{R} : \nabla \mathbf{V}_A \\ & - 2\epsilon_m \cdot (\nabla \times \mathbf{u}) + (\mathbf{V}_A \cdot \nabla) Z^2 \\ & - (1 - \sigma_D) Z^2 \nabla \cdot \mathbf{V}_A - \frac{\alpha f^-(\sigma_c) Z^3}{\lambda}, \end{aligned} \quad (19)$$

$$\frac{\partial \lambda}{\partial t} + (\mathbf{v} \cdot \nabla) \lambda = \beta f^+(\sigma_c) Z, \quad (20)$$

where $Z^2 = \langle v'^2 \rangle + \langle b'^2 \rangle$ is twice the fluctuation energy per unit mass, with $\mathbf{b}' = \mathbf{B}'(4\pi\rho)^{-1/2}$; $\sigma_c = 2\langle \mathbf{v}' \cdot \mathbf{b}' \rangle Z^{-2}$ is the normalized cross helicity; λ is the correlation scale; $\sigma_D = (\langle v'^2 \rangle - \langle b'^2 \rangle) Z^{-2}$ is the normalized energy difference; $\mathbf{V}_A = \mathbf{B}(4\pi\rho)^{-1/2}$ is the mean Alfvén velocity; α and β are the Kármán–Taylor constants; and

$$f^\pm(\sigma_c) = \frac{1}{2}(1 - \sigma_c^2)^{1/2}[(1 + \sigma_c)^{1/2} \pm (1 - \sigma_c)^{1/2}] \quad (21)$$

is a function of σ_c (Matthaeus et al. 2004), which modifies the nonlinear decay phenomenology if $\sigma_c \neq 0$. The terms with \mathcal{R} are the double inner products of the Reynolds stress tensor and the flow or Alfvén velocity gradient tensor. The mean turbulent magnetic field energy can be expressed as $\langle B'^2 \rangle / 8\pi = (1 - \sigma_D) \rho Z^2 / 4$.

In this study we continue treating the normalized energy difference σ_D as a constant parameter. This simplification is justified primarily by solar wind observations that show that the Alfvén ratio r_A is often close to 0.5 (Matthaeus & Goldstein 1982; Tu & Marsch 1995). The corresponding $\sigma_D = (r_A - 1)/(r_A + 1)$ is $-1/3$, which is the value we use below. In general, the evolution of σ_D should be described by a separate equation (Zhou & Matthaeus 1990; Tu & Marsch 1993; Yokoi et al. 2008; Zank et al. 2012). However, due to a number of challenges in modeling σ_D (Grappin et al. 1983; Matthaeus et al. 1994; Hossain et al. 1995), we leave this improvement for future studies.

The rightmost term in Equation (18) is a phenomenological approximation for the transformation rate of turbulence energy into internal energy (see Breech et al. 2008). Consequently, the energy supply due to turbulence in Equations (4)–(5) has the form

$$Q_T = \frac{\alpha f^+(\sigma_c) \rho Z^3}{2\lambda}. \quad (22)$$

2.5. Approximations for the Reynolds Stress Tensor

Under the assumption of structural similarity, along with the presumption that the polarization of the turbulence is transverse to the mean magnetic field \mathbf{B} and axisymmetric about \mathbf{B} , the Reynolds stress tensor can be reduced to

(Usmanov et al. 2009, 2011, 2012, 2016)

$$\frac{1}{\rho} \mathcal{R} = K_R (\mathbf{I} - \hat{\mathbf{B}} \hat{\mathbf{B}}), \quad (23)$$

where $K_R = (\langle v'^2 \rangle - \langle b'^2 \rangle)/2 = \sigma_D Z^2/2$ is the residual energy and $\hat{\mathbf{B}}$ is a unit vector in the direction of \mathbf{B} . Another form of \mathcal{R} employed by Usmanov et al. (2014) is based on the eddy viscosity approximation. It accounts for driving of turbulence by large-scale velocity gradients and can be written (Yoshizawa 1998; Biskamp 2003; Yokoi et al. 2008; Usmanov et al. 2014) as

$$\frac{1}{\rho} \mathcal{R} = \frac{2}{3} K_R \mathbf{I} - \nu_K \mathcal{S} + \nu_M \mathcal{M}, \quad (24)$$

where ν_K and ν_M are the eddy viscosity coefficients and \mathcal{S} and \mathcal{M} are symmetric traceless tensors that represent the strain rates of the mean velocity \mathbf{u} and the mean Alfvén velocity \mathbf{V}_A , respectively,

$$\mathcal{S} = \nabla \mathbf{u} + \nabla \mathbf{u}^T - \frac{2}{3} (\nabla \cdot \mathbf{u}) \mathbf{I}, \quad (25)$$

$$\mathcal{M} = \nabla \mathbf{V}_A + \nabla \mathbf{V}_A^T - \frac{2}{3} (\nabla \cdot \mathbf{V}_A) \mathbf{I}. \quad (26)$$

The superscript T denotes the matrix transpose operation.

It is straightforward to show that $\nabla \mathbf{v} + \nabla \mathbf{v}^T - (2/3) (\nabla \cdot \mathbf{v}) \mathbf{I} = \nabla \mathbf{u} + \nabla \mathbf{u}^T - (2/3) (\nabla \cdot \mathbf{u}) \mathbf{I}$ and therefore the \mathcal{S} tensor is invariant with respect to frame rotations. The same is true for the \mathcal{M} tensor since the magnetic field vector is the same in the rotating and inertial frames. In this paper we will use the following form of \mathcal{R} that smoothly interpolates between Equations (23) and (24):

$$\frac{1}{\rho} \mathcal{R} = \frac{2}{3 - \alpha_T} K_R (\mathbf{I} - \alpha_T \hat{\mathbf{B}} \hat{\mathbf{B}}) - \nu_K \mathcal{S} + \nu_M \mathcal{M}, \quad (27)$$

where α_T is a parameter that takes values between 0 and 1. If $\alpha_T = 0$, then Equation (24) is recovered, and $\alpha_T = 1$ leads to Equation (23) if $\nu_K = \nu_M = 0$. Since \mathcal{S} and \mathcal{M} are symmetric tensors, \mathcal{R} is also symmetric. The terms with \mathcal{R} in Equations (18)–(19) can be written then as

$$\begin{aligned} \frac{1}{\rho} \mathcal{R} : \nabla \mathbf{u} &= \frac{2}{3 - \alpha_T} K_R [\nabla \cdot \mathbf{u} - \alpha_T \hat{\mathbf{B}} \cdot (\hat{\mathbf{B}} \cdot \nabla) \mathbf{u}] \\ &\quad - \frac{1}{2} (\nu_K \mathcal{S} : \mathcal{S} - \nu_M \mathcal{S} : \mathcal{M}) \end{aligned} \quad (28)$$

and

$$\begin{aligned} \frac{1}{\rho} \mathcal{R} : \nabla \mathbf{V}_A &= \frac{2}{3 - \alpha_T} K_R [\nabla \cdot \mathbf{V}_A - \alpha_T \hat{\mathbf{B}} \cdot (\hat{\mathbf{B}} \cdot \nabla) \mathbf{V}_A] \\ &\quad - \frac{1}{2} (\nu_K \mathcal{S} : \mathcal{M} - \nu_M \mathcal{M} : \mathcal{M}). \end{aligned} \quad (29)$$

The two-scale direct-interaction approximation (TSDIA) formalism of Yoshizawa (1984, 1998) relates the eddy viscosity coefficients in Equation (24) and those in the approximation for the mean turbulent electric field

$$\varepsilon_m = \bar{\alpha} \mathbf{B} - \bar{\beta} \nabla \times \mathbf{V}_A + \bar{\gamma} \nabla \times \mathbf{v}, \quad (30)$$

as $\nu_K = (7/5) \bar{\beta}$ and $\nu_M = (7/5) \bar{\gamma}$. The coefficients $\bar{\beta}$ (the turbulent resistivity or magnetic resistivity) and $\bar{\gamma}$ are modeled in TSDIA as $\bar{\beta} = C_\beta K^2 / \varepsilon$ and $\bar{\gamma} = C_\gamma K W / \varepsilon$, where $K = (\langle v'^2 \rangle + \langle b'^2 \rangle)/2 = Z^2/2$ is the turbulence energy per unit

mass, and $W = \langle \mathbf{v}' \cdot \mathbf{b}' \rangle = \sigma_c Z^2/2$ is the cross helicity. Usmanov et al. (2014) approximated the mean turbulent energy dissipation rate ε as $\varepsilon = 2 C_\varepsilon Z^3 / 9 \sqrt{3} \lambda$, where $C_\varepsilon \approx 0.5$. The constants C_β and C_γ were estimated by Yoshizawa (1998) as 0.05 and 0.04, respectively. Then, the eddy viscosity coefficients can be calculated as

$$\nu_K = \frac{63 \sqrt{3}}{40} \frac{C_\beta}{C_\varepsilon} Z \lambda, \quad \nu_M = \frac{63 \sqrt{3}}{40} \frac{C_\gamma}{C_\varepsilon} \sigma_c Z \lambda, \quad (31)$$

or $\nu_K \approx 0.27 Z \lambda$ and $\nu_M \approx 0.22 \sigma_c Z \lambda$.

Since no linear correlation appears to exist in *Helios* data between ε_m and \mathbf{B} (Marsch & Tu 1992), we will neglect the first term (α -effect) in Equation (30). We note here that relations (24) and (30) have been formulated by Yoshizawa (1998) for the case of constant density and, strictly speaking, they are not directly applicable to the expanding solar wind, in which density decreases approximately as r^{-2} . However, if the density fluctuations are neglected, Yokoi (2013) and Yokoi et al. (2013) argue that relations (24) and (30) are still valid.

2.6. The Two-region Numerical Approach

We solve the Reynolds-averaged mean-flow Equations (1) (4)–(5), and (10)–(11) concurrently with the turbulence transport Equations (18)–(20) in the spherical shell between the base of solar corona (just above the transition region) and the heliocentric distance of 5 au. The complete set of equations in a nondimensional component form is given in Appendix B. The computational domain is split into two regions: the inner (coronal) region of 1–30 R_\odot and the outer (solar wind) region from 30 R_\odot to 5 au. The relaxation method, i.e., the integration of time-dependent equations in time until a steady state is achieved, is used in both regions. The location of the boundary between the two regions was arbitrarily chosen to satisfy the condition that the flow is supersonic and super-Alfvénic on the boundary. This implies that no disturbances can propagate inward from the boundary. Consequently, the solution in the inner region is independent of the solution in the outer region. In the inner region, the typical time of integration is 48 hr in physical time, but the changes in the solution are small after ~ 30 hr. The typical integration time in the outer region is 600 hr, or 25 days. Recall that the governing equations are solved in the rotating coordinates and achieving a steady state means that the solution becomes stationary in the rotating frame.

Identical equations are solved in both regions, but the magnetic field is decomposed into potential and nonpotential parts only in the inner region. In the outer region, the impact of the magnetic field on the flow is relatively weak and the equations are solved for the total field \mathbf{B} by formally setting $\mathbf{B}_0 = 0$ and $\mathbf{B}_1 = \mathbf{B}$. In addition, in the inner region, where the magnetic field is strong and its potential component dominates, we compute the rate-of-strain \mathcal{M} tensor based on the deviation field \mathbf{B}_1 rather than the total field \mathbf{B} . This adjustment is based on the well-known fact that in regions of large-scale shear supported by external conditions (Lévêque et al. 2007; Xia et al. 2015) the unmodified effects of the eddy viscosity/Reynolds stresses are too large. In these prior works, the solution offered is to reduce the eddy viscosity. In the present study, we have relevant information, namely, that part of the field is potential, and that part is supported by boundary conditions. Therefore, only the energy in the nonpotential part, \mathbf{B}_1 , is available to drive the unresolved cascade. Computing the rate-of-strain tensor \mathcal{M} including only \mathbf{B}_1 is a physically motivated way to exclude this unavailable energy in the potential field \mathbf{B}_0 .

We solve the governing equations in spherical coordinates on a composite grid consisting of three overlapping spherical fragments (Usmanov 1996; Usmanov et al. 2012). The composite grid approach makes it possible to avoid the geometrical singularity on the polar axis and the shrinking of grid cells along the azimuthal direction as one approaches the poles. To increase the radial grid resolution in the region near the Sun, we use a logarithmic transformation of the radial coordinate r to a new coordinate $r' = \ln(r/r_0)$, where $r_0 = 1 R_\odot$ (Usmanov 1993a). If the grid spacing $\Delta r'$ along r' is constant, Δr increases linearly as a function of r . In the inner region, the grid used in this study consists of 308 points distributed equidistantly along r' . Correspondingly, the grid resolution in r increases from $\sim 0.01 R_\odot$ at the inner boundary to $\sim 0.3 R_\odot$ at the inter-region boundary of $30 R_\odot$. In the outer region, the radial grid of 400 points also employs the logarithmic spacing, with Δr increasing from 0.3 to $9.6 R_\odot$. The angular spacing is set to 1.5° in both regions. However, to save computer resources, a lower-resolution grid with 154 radial points and 3° angular spacing was used for the parametric studies described in Section 3.

To integrate the equations numerically, we use the Central Weighted Essentially Non-Oscillatory (CWENO) semi-discrete method of Kurganov & Levy (2000), which is a shock-capturing third-order-accurate finite-volume scheme based on piecewise polynomial reconstructions and local smoothness indicators. To advance solutions in time explicitly, the strong stability-preserving Runge–Kutta time integration scheme of Gottlieb et al. (2001) is used. The polynomial reconstruction in the CWENO scheme is computed dimension by dimension as a linear combination of two linear and one quadratic approximations with the weights assigned depending on the local smoothness of the solution. The weighting works so that the quadratic approximation dominates in smooth regions, while the linear polynomials take the lead in nonsmooth regions. This allows one to achieve high-order accuracy with nonoscillatory behavior near discontinuities, while avoiding costly computations based on a Riemann solver. The eight-wave scheme of Powell et al. (1999) is used to maintain the $\nabla \cdot \mathbf{B} = 0$ condition by adding source terms proportional to $\nabla \cdot \mathbf{B}$ to the momentum and induction equations so that magnetic monopoles are advected with the flow.

2.7. Conservative versus Nonconservative Forms of the Energy Equations

Recently, Pogorelov et al. (2016, 2017a, 2017b) criticized Usmanov et al. (2016) for using a so-called nonconservative form for the energy equations. In particular, Pogorelov et al. (2016) state, “It is understood that only the fundamental physical conservation laws are appropriate for the description of magnetized fluid flows. In contrast, Usmanov et al. (2016) solve nonconservative pressure equations everywhere in the [solar wind–local interstellar medium] interaction region, which violates the basic principles required to solve systems of hyperbolic equations.” In addition, Pogorelov et al. (2017a) state (again without justification), “Approaches that are not based on the conservation law principles and involving straightforward calculations of the [pickup ion] pressure derivatives across the [termination shock] (e.g., Usmanov et al. 2016) are mathematically flawed.”

A critical circumstance that directly justifies our choice of nonconservative pressure equations is that the governing equations cannot be cast into a fully conservative form *in principle*. It is straightforward to replace an internal energy (pressure) equation with a total energy equation (obtained by manipulating the

continuity, moment, induction, and internal energy equations) in a *single-fluid* case (e.g., Usmanov et al. 2011). However, it is impossible to transform the governing equations into a fully conservative form (and therefore to attain a conservative discretization) if the equations are multifluid and are coupled through the magnetic field (Tóth et al. 2012; Zieger et al. 2015). The mean-flow equations in Usmanov et al. (2016) and in this paper are *multifluid*, and they cannot be rewritten in a fully conservative form. While it is possible to replace, e.g., the pressure equation for protons (4) with the total energy equation, the electron pressure Equation (5) would still retain a nonconservative form. (A similar situation obtains with the two-fluid system of equations in, e.g., Pogorelov et al. [2016], where the equation for thermal pressure is written in a nonconservative form.)

Another issue with the fully conservative form of equations arises if a turbulence model is coupled with mean-flow (Reynolds-averaged) equations. There is simply no guarantee that turbulence equations can be written in a conservative form. As a result, only a *quasi-conservative* form (with the spatial derivatives still appearing in the source terms) has been employed for turbulence equations by Usmanov et al. (2009, 2011, 2012, 2014, 2016) and also by Kryukov et al. (2012) and Wiengarten et al. (2014, 2016). (Note that although the turbulence equations in Kryukov et al. [2012] appear to be in conservative form, the equation for turbulent energy contains a mixing term $[-\sigma_D M_1 \rho Z^2]$ with the spatial derivatives [hidden in M_1] on the right-hand side. In addition, the equations for turbulent energy and cross helicity can be cast in the conservative form given in Kryukov et al. [2012] only if the terms $\rho Z^2 \nabla \cdot \mathbf{u}/2$ and $\rho Z^2 \sigma_c \nabla \cdot \mathbf{u}/2$ are dropped. Furthermore, the governing equations in Kryukov et al. [2012] do not include “a fluid treatment of pickup ions,” in apparent conflict with what is announced in the abstract of the paper.)

In addition, there is a specific difficulty that makes the conservative form troublesome and virtually inapplicable in many important applications even in the single-fluid case. Using a total energy equation instead of an equation for thermal (internal) energy involves calculation of thermal pressure at each integration step by subtracting the contributions of other energies from the total energy. If the thermal energy is not significantly (orders of magnitude) smaller than other energy terms, this subtraction poses no problem, and the conservative form is preferable. However, if any other form of energy (e.g., magnetic or kinetic) dominates the thermal energy (the typical situation near the coronal base and beyond $\sim 20 R_\odot$, respectively), it is often impossible to calculate the thermal energy accurately because the calculation involves numerous subtractions of large and nearly equal quantities. The problem is often discussed in the context of “positivity” of thermal pressure that at times can become negative as a result of the subtraction, with some algorithms especially designed to preserve the “positivity” (e.g., Einfeldt et al. 1991; Hu & Khoo 2003). However, “positivity” does not generally guarantee accuracy and therefore might not be sufficient.

Thus, although the conservative form of the energy equation is generally preferable for MHD problems with shocks in computational domains, experience has shown that the conservative form of the equations can be troublesome in flow regimes where the magnetic or kinetic energy is much larger than the flow internal energy. Moreover, the governing equations used in this paper and, e.g., by Usmanov et al. (2016) simply cannot be cast in a fully conservative form because they are multifluid and coupled with turbulence transport equations. Meanwhile, the mass, momentum, and induction equations are all solved in the conservative form. It

Table 1
Summary of the Model Parameters

Symbol	Description	Value
N_0	Number density of protons and electrons in the initial state at $1 R_\odot$	$8 \times 10^7 \text{ cm}^{-3}$
T_0	Temperature of electrons and protons in the initial state at $1 R_\odot$	$1.8 \times 10^6 \text{ K}$
B_0	Magnetic field strength of a dipole on the pole at $1 R_\odot$	12 G
γ	Ratio of specific heats (adiabatic index)	5/3
r_H	Collisional/collisionless electron heat flux transition radius	$5 R_\odot$
α_H	Constant in Hollweg's collisionless heat flux approximation	1.05
δv_0	Driving amplitude of velocity fluctuations at $1 R_\odot$	28.6 km s^{-1}
λ_0	Correlation scale of turbulence at $1 R_\odot$	$0.015 R_\odot$
σ_D	Normalized energy difference (residual energy)	-1/3
α_T	Turbulence anisotropy parameter	1
α, β	Kármán–Taylor constants	$\alpha = 2\beta = 0.128$
f_p	Proton turbulent heating fraction	0.6
$C_\beta, C_\gamma, C_\varepsilon$	Turbulence model constants	$C_\beta = 0.05, C_\gamma = 0.04, C_\varepsilon = 0.5$

is instructive to note that a nonconservative form of MHD equations has been successfully used with a shock-capturing method, e.g., by Raeder (2003) and Lyon et al. (2004).

2.8. Initial State and Model Parameters

Typical model parameters are listed in Table 1. The first six parameters are related to the mean-flow equations, and the rest appear in the turbulence transport model. The initial state in the inner region is constructed as a superposition of one-dimensional solutions of solar wind equations with WKB Alfvén waves (Usmanov et al. 2000) in a potential magnetic field for the inner boundary values of number density N_0 , temperature T_0 , driving amplitude of velocity δv_0 , and correlation scale λ_0 listed in Table 1. In the initial state, the correlation scale λ was chosen to increase linearly with distance, and the cross helicity is set as $\sigma_c = -\sigma_{c0} B_r / B_r^{\max}$, where $\sigma_{c0} = 0.8$, B_r is the radial magnetic field, and B_r^{\max} is the maximum absolute value of B_r on the inner boundary. Spherical coordinates (r, θ, ϕ) with the polar axis along the solar rotation axis Ω are used. We assume that solar wind heating comes from the turbulent cascade and the electron heat flux and that the adiabatic index $\gamma = 5/3$. The parameter r_H that defines the radius of transition from the collisional to collisionless heat flux (17) is taken to be $5 R_\odot$, the constant in the collisionless electron heat flux approximation (15) $\alpha_H = 1.05$, and the turbulence anisotropy parameter $\alpha_T = 1$. Following Usmanov et al. (2014), the normalized energy difference $\sigma_D = -1/3$; the fraction of turbulent energy absorbed by protons $f_p = 0.6$; the turbulence model constants $C_\beta = 0.05$, $C_\gamma = 0.04$, and $C_\varepsilon = 0.5$; and the Kármán–Taylor constants $\alpha = 2\beta = 0.128$. The choice $\alpha = 2\beta$ corresponds to a similarity decay of the de Kármán & Howarth (1938) type, which requires that the turbulent viscosity also follows a similarity solution. See discussion in Dryden (1943) and Matthaeus et al. (1996).

2.9. Boundary Conditions

In the method of projected characteristics (e.g., Nakagawa & Steinolfson 1976; Wang et al. 1982; Hu & Wu 1984; Thompson 1990), the number of dependent variables that can be specified arbitrarily at a boundary is equal to the number of incoming normal characteristics, which start from the boundary and enter the computational domain. Other dependent variables must be determined from the differential equations (compatibility relations) along the outgoing characteristics, which go to the boundary from the computational domain.

In a single-fluid ideal MHD case without turbulence, the governing system of equations consists of eight scalar equations. Correspondingly, the eigenvalue analysis of the equations shows that there are eight characteristic velocities. If the flow speed is smaller than the slow-magnetosonic speed and the flow is directed from the boundary, five characteristics are incoming and three are outgoing. The former correspond to the slow-magnetosonic, Alfvén, and fast-magnetosonic waves propagating downstream and two entropy waves advected at flow speed. The three incoming characteristics are the fast-magnetosonic, Alfvén, and slow-magnetosonic waves propagating upstream. In a two-fluid case with separate energy equations for protons and electrons (nine scalar equations in total), there are still three incoming characteristics, but six outgoing. The number of entropy waves in this case is three, and the magnetosonic speeds are calculated based on the total pressure of protons and electrons.

To determine the number of incoming and outgoing characteristics for the system of 12 scalar Equations (1)–(5), (10)–(11), (18)–(20) including three turbulence equations, an eigenvalue analysis of the equations is also required. However, because this task is mathematically too cumbersome, we assume in this study that adding the turbulence equations increases the number of outgoing characteristics only by one, so that there are four outgoing and eight incoming characteristics. Therefore, four dependent variables can be computed from flow parameters near the boundary using the compatibility relations, while the other eight can be prescribed at our discretion. Our model employs a simple linear extrapolation as a substitute for the full compatibility relations (Nakagawa & Steinolfson 1976; Steinolfson et al. 1982).

The four variables that we extrapolate back to the boundary are the tangential magnetic field components B_θ and B_ϕ , the cross helicity σ_c , and either the radial velocity u_r or the proton pressure P_S (the electron P_E and proton P_E pressure are assumed to be equal on the boundary). We extrapolate u_r whenever $u_r > 0$ at the boundary; however, when its extrapolated value goes negative, u_r is then fixed to zero and P_S is extrapolated (P_S is fixed to its initial value whenever $u_r > 0$). The boundary values of nonradial velocity components are specified from the condition $\mathbf{v} \parallel \mathbf{B}$, i.e., $u_\theta = u_r B_\theta / B_r$ and $u_\phi = u_r B_\phi / B_r + w_\phi$. The turbulent electric field ε_m is assumed to be negligible on the boundary. The surface density ρ is determined from the relation $P_S / \rho^\gamma = \text{const}$. B_r , Z^2 , and λ are fixed to the initial values. See Table 1.

The boundary between the inner and outer regions is a computational boundary and is placed at the distance where the flow is already supersonic and super-Alfvénic. Consequently, on

the inner boundary of the outer region all characteristics (projected on the radial direction) are incoming, which enables us to fix all dependent variables to the values taken from the outer boundary of the inner region. The outer boundaries of both inner and outer regions are assumed to be of open type with a linear extrapolation applied to all variables (all the characteristics on these boundaries are outgoing).

3. Simulation Results and Analysis

3.1. Dipole Field

To a first and rough approximation, the coronal magnetic field can be represented by a dipole tilted with respect to the solar rotation axis. Near solar activity minimum, the tilt is relatively small, so the dipole is nearly perpendicular to the helioequatorial plane. The tilt varies with solar activity, and it is more substantial during other phases of the solar cycle. The exception is a period around solar maximum when higher harmonics are dominant and the dipole approximation is not feasible. Aiming to compare our simulation results with *Ulysses* data during its first fast latitude transit (FLT) in 1994–1995, we chose the dipole tilt of 10° , which matches approximately the dipole orientation inferred from synoptic magnetograms at the Wilcox Solar Observatory during that period. The strength of the dipole B_0 is taken to be 12 G on the pole at $1 R_\odot$ and has been adjusted to fit the *Ulysses* data. The other parameters are listed in Table 1. The eddy viscosity is switched off by default, and its effects will be discussed in Section 3.7.

The results of the simulation are shown in Figures 1 and 2 as contour maps in a meridional plane for the inner and outer region, respectively. A bimodal structure with a strong latitudinal variation of radial velocity is clearly seen in Figures 1(a) and 2(a). The wind is relatively slow, dense, and cold around the magnetic equator (tilted by $\sim 10^\circ$ with respect to the heliographic equator) and relatively fast, tenuous, and hot at higher latitudes. As can be seen in Figures 1(d) and 2(d), the turbulence energy Z^2 is increased in the fast wind, which is obviously related to its acceleration. The normalized cross helicity σ_c is high everywhere except near the current sheet, which appears as a thin dark region around the equator in Figures 1(c) and 2(c). The cross helicity is also close to zero in the dead zones at the base of the current sheet, where the magnetic field is closed and there is no plasma outflow. In this region, both electron and proton temperatures are enhanced, as can be seen in Figures 1(g) and (h).

Figures 1(f) and 2(f) show that the correlation scale λ is increased in slow wind and is notably smaller at higher latitudes. It should be noted that the computed behavior of λ is opposite to the latitudinal variation assumed by Breech et al. (2008) and also by Usmanov et al. (2009, 2011, 2012, 2014) and Wiengarten et al. (2015, 2016), who set λ at their inner boundary of 0.3 au to be small in the near-equatorial slow wind and to increase poleward. The profile of λ computed in the present study is presumably more realistic because it is computed self-consistently, starting from a uniform distribution of λ on the inner boundary.

At the coronal base, the open-field regions with plasma outflow (the computed “coronal holes”) are located poleward of $\sim 45^\circ$ – 60° in latitude, while the closed-field structures that suppress plasma outflow occupy lower latitudes. The plasma flowing outward from each of the polar “coronal holes” expands super-radially bounded by the closed-field regions. The two polar flows expand until they fill the hemispheres above the closed-field regions. The plot of meridional velocity u_θ in Figure 1(i) demonstrates that the coronal plasma flow is highly nonradial and has a strong component

(up to 60 km s^{-1}) directed toward the equator in both the northern and southern hemispheres.

3.2. Comparison with Ulysses Observations

Figure 3 shows a comparison of the simulation run for the source dipole tilted by 10° with observations by *Ulysses* during its first FLT in 1994–1995 when the heliographic latitude of *Ulysses* varied from -80.2° to $+80.2^\circ$ and its heliocentric distance varied from 1.3 to 2.3 au. It is clear from Figure 3 that there is an overall agreement between the computed and observed parameters in each plot for both latitude and intensity variations, except for the electron temperature. The computed electron temperature in the slow wind is not substantially different from that observed by *Ulysses*, but it is ~ 3 times larger than that observed in the fast wind. Meanwhile, the proton temperature generally matches the “*T*-large” estimate of the observed proton temperature, and the general variations of other plasma and magnetic field parameters are reproduced relatively well.

3.3. Characteristic Surfaces

Figure 4 shows contour plots in a meridional plane of the Mach number M , Alfvén Mach number M_A , and plasma beta parameter β_T calculated based on the total pressure of electrons and protons. The thick white lines are the meridional cross sections of the sonic surface $M = 1$, the Alfvén surface $M_A = 1$, and the $\beta_T = 1$ surface. The behavior of the sonic and Alfvén surfaces in fast and slow wind is notably different. In the fast wind, the sonic surface comes closer to the solar surface than the Alfvén one, while in the slow wind (and especially near the current sheet, where the magnetic field is weak and hence Alfvén velocity is low), the location of surfaces is opposite. The range of distances for the sonic surface is ~ 4 – $12 R_\odot$ and for the Alfvén surface is ~ 7 – $18 R_\odot$. The range of distances for the $\beta_T = 1$ surface is significantly larger, so the β_T plots are shown in two scales in Figures 4(c) and (d). Approaching the Sun as close as $\sim 3.5 R_\odot$ in the slow wind, the $\beta_T = 1$ surface moves outward as far as $\sim 60 R_\odot$ in the fast wind. For more details on these important surfaces, see Chhiber et al. (2018a, 2018b).

3.4. Scaling of WSO Magnetograms

In this study, we also use synoptic magnetograms from Wilcox Solar Observatory to assign boundary conditions for the magnetic field at the coronal base. Riley et al. (2014) have demonstrated that although the synoptic magnetograms from various ground- and space-based observatories are qualitatively similar, the differences in values (as compared by a pixel-by-pixel or histogram-equating technique) can be as large as an order of magnitude. In general, the fields measured at Wilcox Solar Observatory are notably weaker than those from other observatories by a factor ranging from ~ 2 for Mount Wilson Observatory to as high as ~ 12 for *SOHO*/MDI synoptic maps. The fact that WSO fields appear to be too weak when extended to 1 au using a PFSS model led Svalgaard et al. (1978) to introduce a scaling factor of 1.8 for WSO magnetograms. Similarly motivated studies have inferred scaling factors of 2–4 (Ulrich 1992), 1.8 and 3.6 (Zhao & Hoeksema 1995), 1.85 (Svalgaard 2006), and 2.0 (Cohen et al. 2007).

In view of these discrepant results vis-à-vis the WSO magnetic field scaling, we ran our model for a number of scaling factors and compared the results with *Ulysses* data during its first and third FLTs in 1994–1995 and 2007–2008, respectively. Both time periods are around solar minima with a relatively stationary

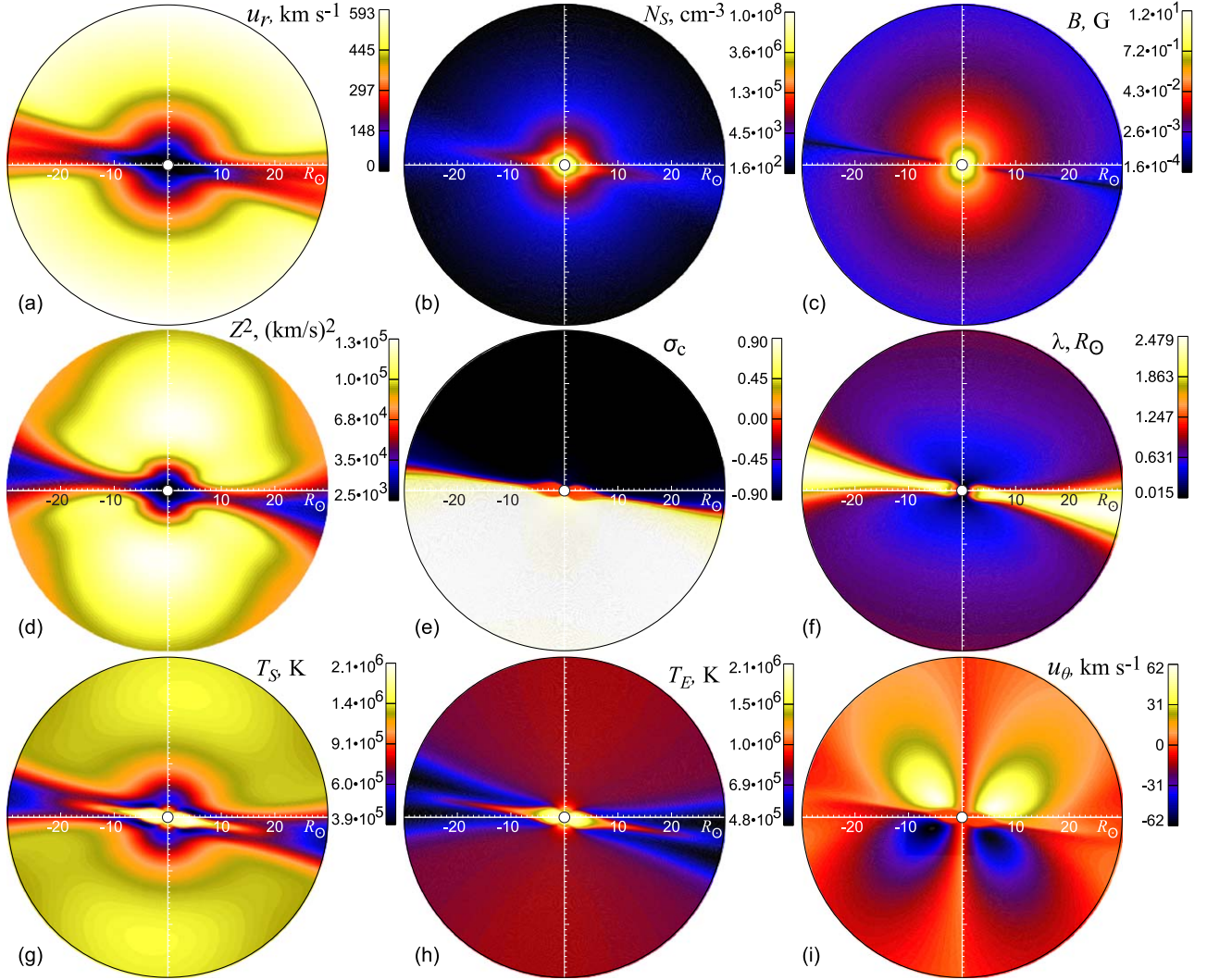


Figure 1. Color plots of the plasma, magnetic field, and turbulence parameters in the inner region ($1\text{--}30 R_{\odot}$) in the meridional plane $\phi = 0^{\circ}75$: (a) radial velocity u_r , (b) proton density N_S , (c) magnetic field magnitude B , (d) turbulence energy per unit mass Z^2 , (e) cross helicity σ_c , (f) correlation scale λ , (g) proton temperature T_S , (h) electron temperature T_E , and (i) meridional velocity u_{θ} . The heliocentric distance is in solar radii.

solar wind structure. Although both time intervals are about 11 months long, the simulations have been done for a particular Carrington rotation (CR) during each of the intervals, CR 1898 and CR 2078, respectively, under the assumption that the solar wind structure did not change substantially during the *Ulysses* transits. Figure 5 compares the simulation results with *Ulysses* observations for three scaling factors 4, 6, and 8 for the first interval and 6, 8, and 10 for the second one. The most noteworthy result is that the scaling does not significantly change the model results along the *Ulysses* orbit. The changes are particularly small for the magnetic field components even though the field at the coronal base doubles. An obvious explanation for this effect is that the stronger field leads to larger dead zones near the Sun, where the magnetic field is closed, and, consequently, to smaller open-field flux. Meanwhile, the changes in plasma parameters are more pronounced, with the best agreement, on average, for scaling factors 6 and 8, respectively. Figure 5 does not include a plot for electron temperature, as there are no *Ulysses* data on electron temperature for the third FLT. For the first FLT, the computed electron temperature in fast solar wind is still too high, and similar to what is shown in Figure 3 for the dipole case.

3.5. Effects of the Base Temperature T_0

Figure 6 shows profiles of plasma and turbulence parameters along a radial line at the north pole for a series of runs with an untitled dipole for various values of plasma temperature at the coronal base T_0 . As T_0 increases from 1.6×10^6 K to 2.4×10^6 K, the radial velocity u_r decreases and the proton density N_S increases, from ~ 900 to 400 km s^{-1} and from 1.4 to 19 cm^{-3} , respectively, at 1 au. A striking feature of the proton T_S and electron T_E temperature profiles in Figures 6(b) and (c) is that higher T_0 leads to smaller temperatures beyond $\sim 3\text{--}4 R_{\odot}$. The respective drop in proton temperature at 1 au is from 4.6×10^5 K to 8.1×10^4 K. The proton temperature shows a broad maximum around $20\text{--}30 R_{\odot}$, which is obviously related to the maximum of Z^2 in Figure 6(d). The turbulence energy per unit mass has a maximum around $10\text{--}20 R_{\odot}$ and increases when T_0 decreases. The correlation scale λ is virtually independent of T_0 , while the cross helicity σ_c shows a dependence of T_0 only inside $\sim 4 R_{\odot}$.

3.6. Turbulent Energy Production

To explain the seemingly counterintuitive anticorrelation between the temperatures at the coronal base T_0 and at 1 au, let

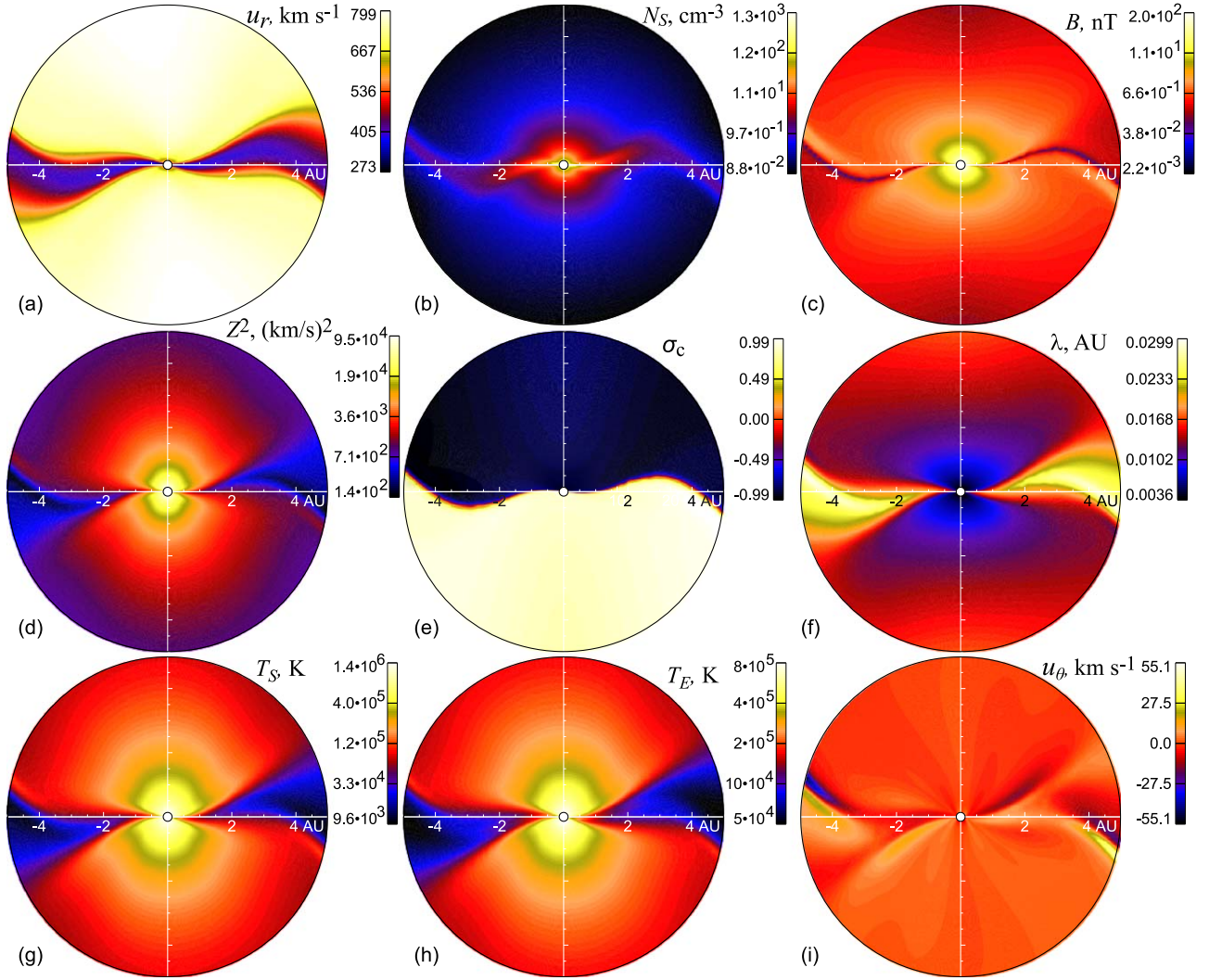


Figure 2. Same as in Figure 1, but in the outer region from $30 R_\odot$ to 5 au. The heliocentric distance is in astronomical units.

us consider the terms in the Z^2 Equation (18). Since the Alfvén velocity is not assumed to be small in comparison with flow velocity, there are terms with V_A on the right-hand side of Equation (18) that did not appear in the turbulence energy equation of Breech et al. (2008). The radial variations from $1 R_\odot$ to 1 au along the pole of the terms on the right-hand side of Equation (18) are shown in Figure 7(a) for the steady-state solution without eddy viscosity. The largest term, which is primarily responsible for the production of turbulence, is $-Z^2 \sigma_c \nabla \cdot \mathbf{V}_A$. Taking into account the identity $\nabla \cdot \mathbf{V}_A = -(\mathbf{V}_A \cdot \nabla) \rho / 2\rho$ and the fact that B_r and σ_c have opposite signs, the term can be rewritten as

$$-Z^2 \sigma_c \nabla \cdot \mathbf{V}_A \approx -\frac{Z^2 |\sigma_c B_r|}{2\rho (4\pi\rho)^{1/2}} \frac{\partial \rho}{\partial r}. \quad (32)$$

Lower temperature at the coronal base leads to faster density decrease with distance, i.e., to larger negative gradient $d\rho/dr$ and, as it follows from Equation (32), to faster increase in Z^2 . The higher Z^2 causes higher turbulent dissipation ($\sim Z^3/\lambda$) that leads to higher temperature.

The radial variations of the terms in Equation (19) along the pole are shown in Figure 7. As the cross helicity is negative at the north pole (see Figure 6(f)), the main $Z^2 \sigma_c$ -production term

is again the one proportional to the divergence of Alfvén velocity: $-(1 - \sigma_D) Z^2 \nabla \cdot \mathbf{V}_A$. Other terms work largely to decrease $Z^2 \sigma_c$.

3.7. Effects of the Kármán–Taylor Constant α , Alfvén Ratio, and Eddy Viscosity

Figure 8 shows the radial variation at the pole of flow and turbulence parameters for a number of values of the Kármán–Taylor constant α , which is a factor in the model for turbulent heating rate (Equation (18)) and also enters as a factor in the nonlinear term describing evolution of cross helicity (Equation (19)). The results appear to be fairly similar, except that the correlation scale λ increases with distance much faster for larger α . Obviously, this is due to larger β , since we use the relation $\alpha = 2\beta$. As a result, the turbulent dissipation rate, which is proportional to α/λ , does not change significantly.

Similar radial profiles are shown for different values of the Alfvén ratio r_A in Figure 9. While N_S virtually does not change and there are few deviations for proton and electron temperatures and turbulence energy, the correlation scale λ is notably smaller and the cross helicity σ_c is notably larger for smaller r_A . The radial velocity is also enhanced for larger r_A .

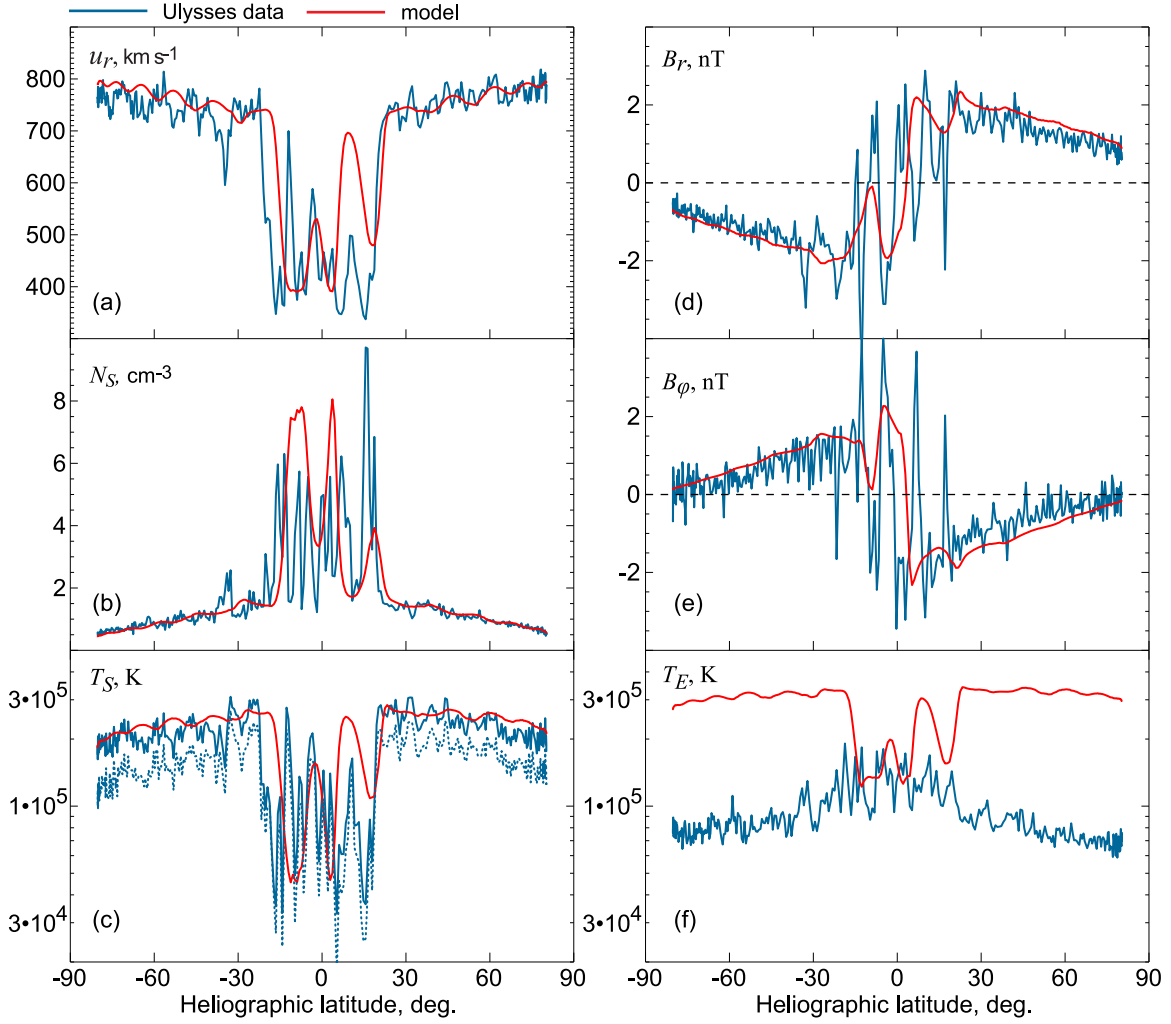


Figure 3. Simulated profiles (red) for a source magnetic dipole on the Sun tilted by 10° (with respect to the solar rotation axis) vs. *Ulysses* daily averages of plasma and magnetic field parameters measured during the first FLT of *Ulysses* (1994 September 13 to 1995 July 31). The parameters shown are (a) the radial velocity u_r , (b) the number density of solar protons N_S and (c) their temperature T_S , (d) the radial B_r and (e) the azimuthal B_ϕ magnetic field components, and (f) the electron temperature T_E . Two estimates, “ T -large” and “ T -small” of the proton temperature measured by *Ulysses*, are shown by blue solid and dotted lines, respectively.

Figure 10 demonstrates latitudinal variations at $30 R_\odot$ (the top of the inner region) of the flow and turbulence parameters for runs with eddy viscosity turned on and off ($\nu_K = \nu_M = 0$). The effect of eddy viscosity is obviously to smooth the gradients and broaden the slow wind region.

3.8. Loss of Angular Momentum

As shown in Appendix A, the loss rate of the angular momentum of the Sun due to the solar wind is the integral over a sphere of arbitrary radius r ,

$$j_\odot = \int_0^\pi \int_0^{2\pi} r^3 \sin^2 \theta \left(\rho u_r u_\phi - \frac{B_r B_\phi}{4\pi} + \mathcal{R}_{r\phi} \right) d\theta d\phi, \quad (33)$$

where u_r and u_ϕ are the radial and azimuthal components of the velocity in the inertial frame and B_r and B_ϕ are the radial and azimuthal components of the magnetic field, respectively. Note that, as demonstrated in Appendix A, the integral is independent of the radius of the sphere. The component of the Reynolds stress tensor (27) contributing to the angular

momentum loss is

$$\mathcal{R}_{r\phi} = -\rho \left[\frac{\sigma_D Z^2 \alpha_T B_r B_\phi}{(3 - \alpha_T) B^2} + \nu_K \mathcal{S}_{r\phi} - \nu_M \mathcal{M}_{r\phi} \right], \quad (34)$$

where

$$\mathcal{S}_{r\phi} = \frac{1}{r \sin \theta} \frac{\partial u_r}{\partial \phi} + r \frac{\partial}{\partial r} \left(\frac{u_\phi}{r} \right) \quad (35)$$

and

$$\mathcal{M}_{r\phi} = \frac{1}{r \sin \theta} \frac{\partial V_{Ar}}{\partial \phi} + r \frac{\partial}{\partial r} \left(\frac{V_{A\phi}}{r} \right). \quad (36)$$

In the absence of eddy viscosity, Equation (33) takes the form

$$j_\odot = \int_0^\pi \int_0^{2\pi} r^3 \sin^2 \theta \left[\rho u_r u_\phi - (1 + \eta) \frac{B_r B_\phi}{4\pi} \right] d\theta d\phi, \quad (37)$$

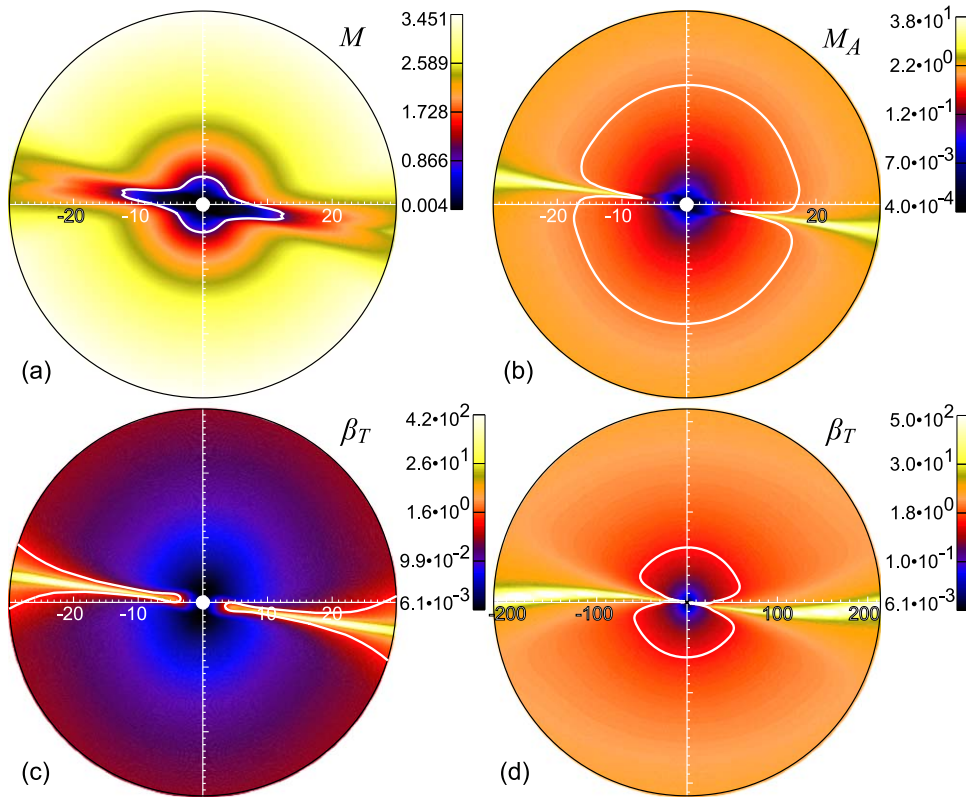


Figure 4. Color plots of the (a) Mach number M , (b) Alfvén Mach number M_A , and (c–d) plasma $\beta_T = 8\pi(P_S + P_E)/B^2$ parameter in the meridional plane $\phi = 0^\circ 75$. The thick white line in each plot is where the respective parameter is equal to 1. The radial range in panels (a)–(c) is from 1 to $30 R_\odot$ and in panel (d) is from $1 R_\odot$ to 1 au.

where η is a function of the model parameters α_T and σ_D and the ratio Z^2/V_A^2 :

$$\eta = \frac{4\pi\sigma_D\alpha_T}{(3 - \alpha_T)} \frac{Z^2}{V_A^2}. \quad (38)$$

The sign of η is determined by the sign of σ_D . The normalized energy difference σ_D measures the difference between the magnetic and kinetic fluctuation energies. Both the data analysis of solar wind observations (e.g., Matthaeus & Goldstein 1982; Tu & Marsch 1995; Podesta et al. 2007) and theoretical studies (e.g., Wang et al. 2011) indicate that the magnetic energy typically exceeds the kinetic energy and hence σ_D is usually negative. Consequently, η is negative as well, and, as one can see from Equation (37), the effect of turbulence is then to decrease the magnetic torque.

Figure 11(a) shows the radial variations of the three components in the torque integral (37) calculated in the outer region ($30 R_\odot$ –5 au) from the simulation run without eddy viscosity ($\nu_K = \nu_M = 0$): plasma \dot{J}_P , magnetic field \dot{J}_M , and turbulence \dot{J}_T contributions, as well as their total, which is indeed virtually constant. The sign of turbulence torque is negative, which means that the turbulence reduces the loss rate of angular momentum or, in other words, facilitates the corotation. The effect is similar to the tendency toward corotation inferred by Weber & Davis (1970) from their one-dimensional model with viscosity and anisotropic pressure. As can be seen from Figure 11(a), the total torque is $\sim 2.5 \times 10^{30}$ erg. On average, the plasma and magnetic torques are approximately equal to 1.6×10^{30} erg, while the turbulent torque is -0.7×10^{30} erg. Thus, the influence of turbulence on the azimuthal momentum loss is significant.

The effect of eddy viscosity on the angular momentum loss is demonstrated in Figure 11(b). It shows the results in the inner region (1 – $30 R_\odot$) from the run with the eddy viscosity. The magnetic torque \dot{J}_M is the dominant component close to the Sun, where the flow speed is low. \dot{J}_M decreases with distance, while the plasma torque \dot{J}_P increases to become comparable with \dot{J}_M beyond $\sim 20 R_\odot$. The turbulent torque \dot{J}_T is again negative, and its effect increases with distance. In addition to the torque components, Figure 11(b) also depicts the contribution from the eddy viscosity \dot{J}_{EV} term, which is small in comparison with the other torque components. Although the direct contribution of \dot{J}_{EV} to the torque integral (33) is small, the influence of eddy viscosity on the angular momentum loss of the Sun is not negligible because the total torque is notably smaller ($\sim 1.4 \times 10^{30}$ erg) for the run with the eddy viscosity than in the run with the eddy viscosity turned off ($\sim 2.5 \times 10^{30}$ erg).

4. Summary and Future Work

We have developed a fully three-dimensional MHD model of the solar corona and solar wind with turbulence transport and heating. The model is based on Reynolds-averaged solar wind equations coupled with transport equations for turbulent quantities. The model accounts for the effects of electron heat conduction, radiative cooling, Coulomb collisions, Reynolds stresses, eddy viscosity, and turbulent heating. Steady-state solutions in the frame of reference rotating with the Sun are constructed using the time relaxation method. The simulation results provide three-dimensional distributions of mean-flow and turbulence parameters between the coronal base and 5 au for given boundary conditions at the coronal base. The computational domain is split into two

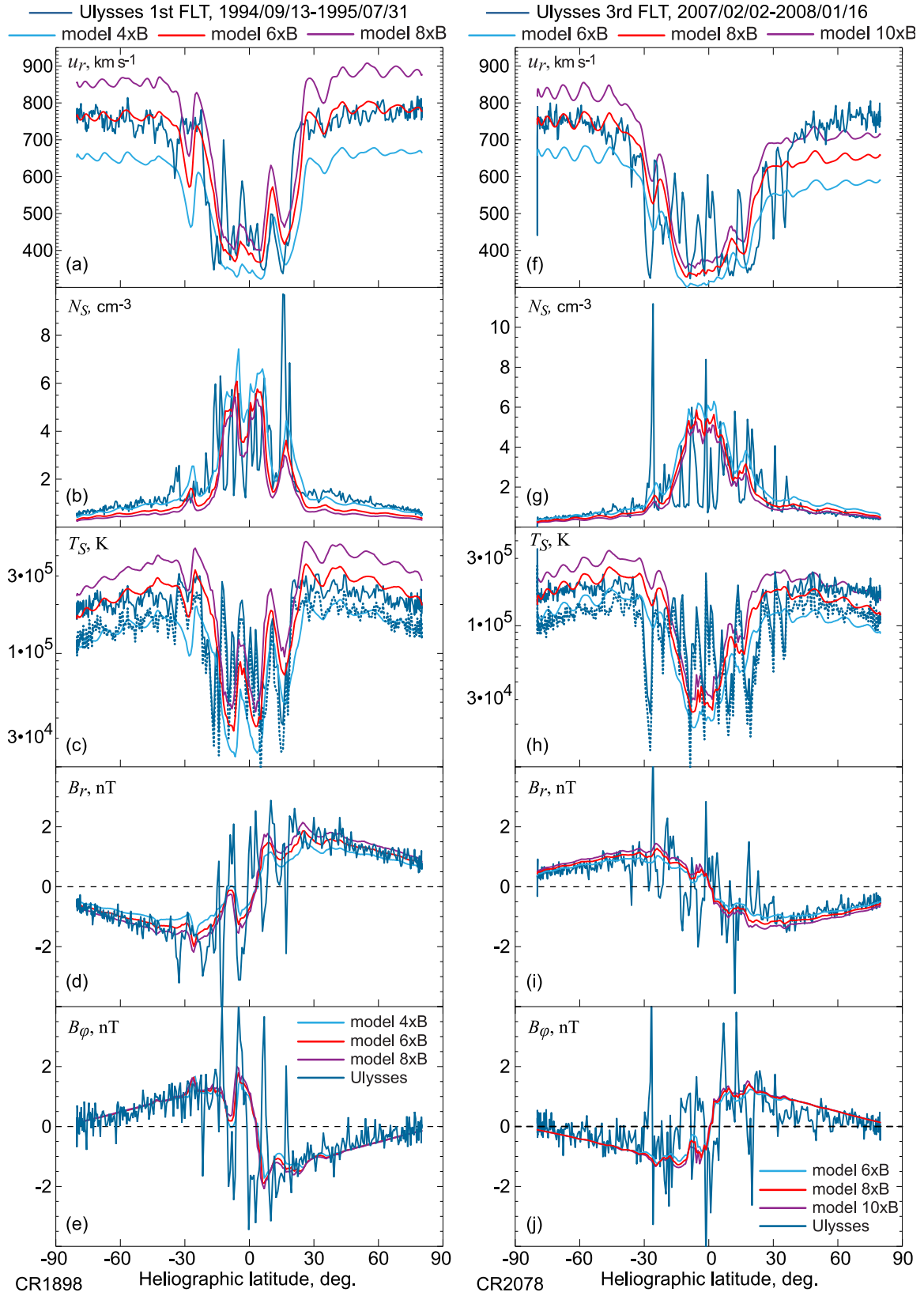


Figure 5. Scaling of magnetograms for CR 1898 (left) and CR 2078 (right) by comparison with *Ulysses* observations during its first and third FLT in 1994–1995 and 2007–2008, respectively. Three scaling factors are used for each interval: 4, 6, and 8 for CR 1898 and 6, 8, and 10 for CR 2078.

regions: $1\text{--}30 R_\odot$ and $30 R_\odot\text{--}1\text{ au}$. Boundary conditions at the coronal base are prescribed using either a tilted/untilted dipole or synoptic solar magnetograms from the Wilcox Solar

Observatory. The strength of the solar dipole and the scaling factor for magnetograms are adjusted by comparison with *Ulysses* observations.

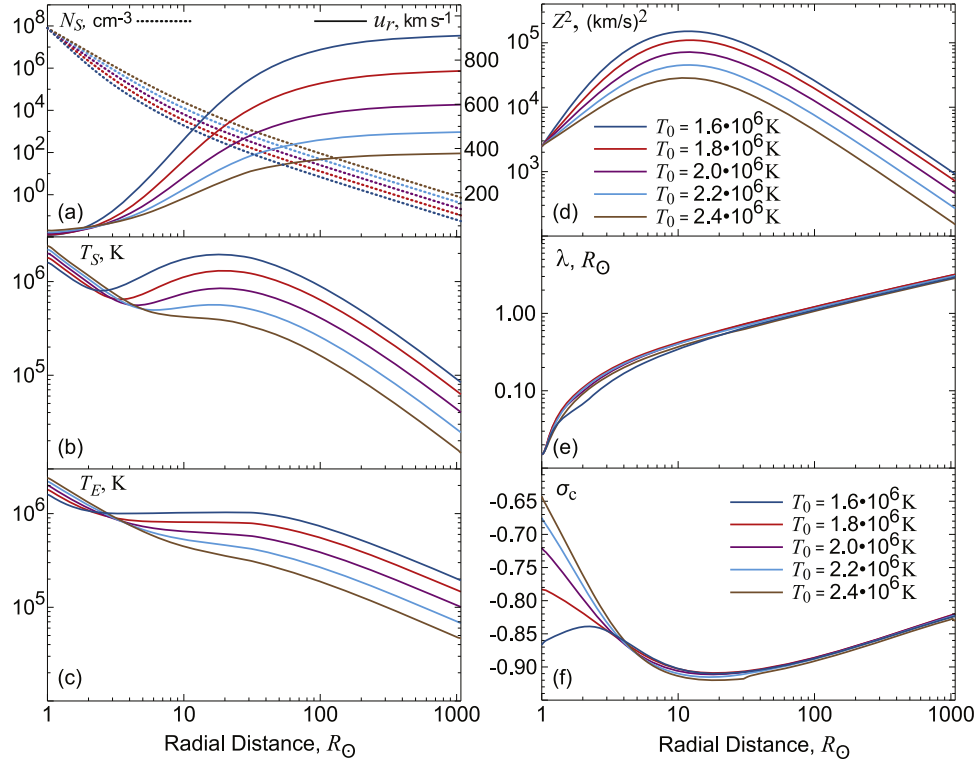


Figure 6. Radial profiles from $1 R_{\odot}$ to 5 au at the pole for various temperatures at the coronal base from $1.6 \times 10^6 \text{ K}$ to $2.4 \times 10^6 \text{ K}$ of (a) the proton density N_S and radial velocity u_r , (b) the proton temperature T_S , (c) the electron temperature T_E , (d) the turbulence energy per unit mass Z^2 , (e) the correlation scale λ , and (f) the cross helicity σ_c . The solar magnetic field is assumed to be an untitled dipole.

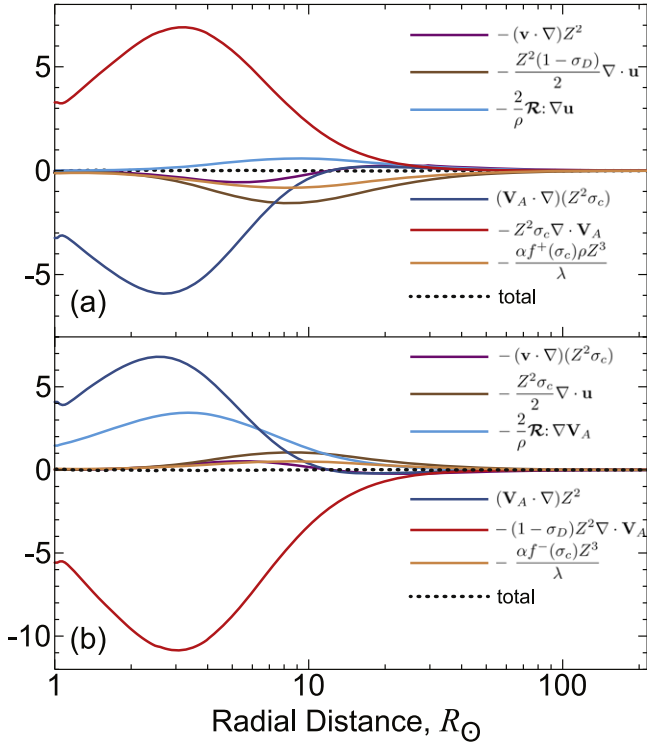


Figure 7. Radial variations from $1 R_{\odot}$ to 1 au at the north pole of the terms in nondimensional units on the right-hand side of (a) Equation (18) and (b) Equation (19). The dotted line shows the total of all the right-hand-side terms in the equations. Note that the eddy viscosity is turned off and, hence, the terms with the turbulent electric field ε_m are equal to zero.

We have shown that the model results compare reasonably well with *Ulysses* observations during *Ulysses*'s first and third FLT's near solar activity minima in 1994–1995 and 2007–2008. The exception is the fast wind electron temperature, which is ~ 3 times higher than that observed by *Ulysses*. We have not found a way to match the observed temperature more closely by varying the boundary conditions at the coronal base or model parameters. This is a topic of ongoing investigation.

An important deficiency of the present model is that the inner boundary is placed above the transition region at a “coronal base,” where the temperature is already above 10^6 K . It is an obvious and important development to expand the computational region by adding the upper chromosphere and transition region. This can be done based on the assumption that the primary source of heating of the solar corona is the turbulent heating (e.g., Matthaeus et al. 1999a; Verdini et al. 2010; Sokolov et al. 2013) using the approach of artificial broadening of the transition region described by Lionello et al. (2009) and Sokolov et al. (2013). The addition of the upper chromosphere and transition region to the computational domain may be helpful in lowering the simulated electron temperature in the fast wind. Also, a computationally simpler approach of setting the density at the inner boundary using the radiative energy balance assumption (Withbroe 1988; Lionello et al. 2001) in combination with lower temperature at the boundary will be tested in future work.

In the studies of Breech et al. (2008), Usmanov et al. (2009, 2011, 2012, 2014), and Wiengarten et al. (2015, 2016), the correlation scale λ was set to increase with latitude from the slow to the fast wind at the inner boundary of 0.3 au . In the present study, λ is computed self-consistently starting from a uniform

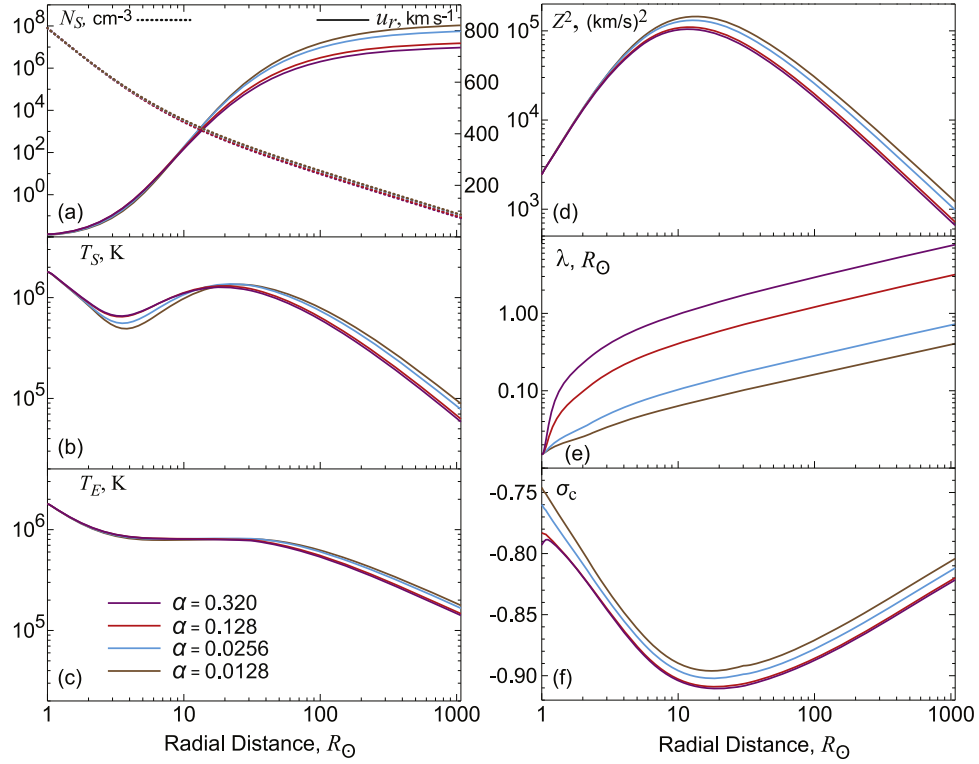


Figure 8. Same as in Figure 6, but for various values of Kármán–Taylor constant α .

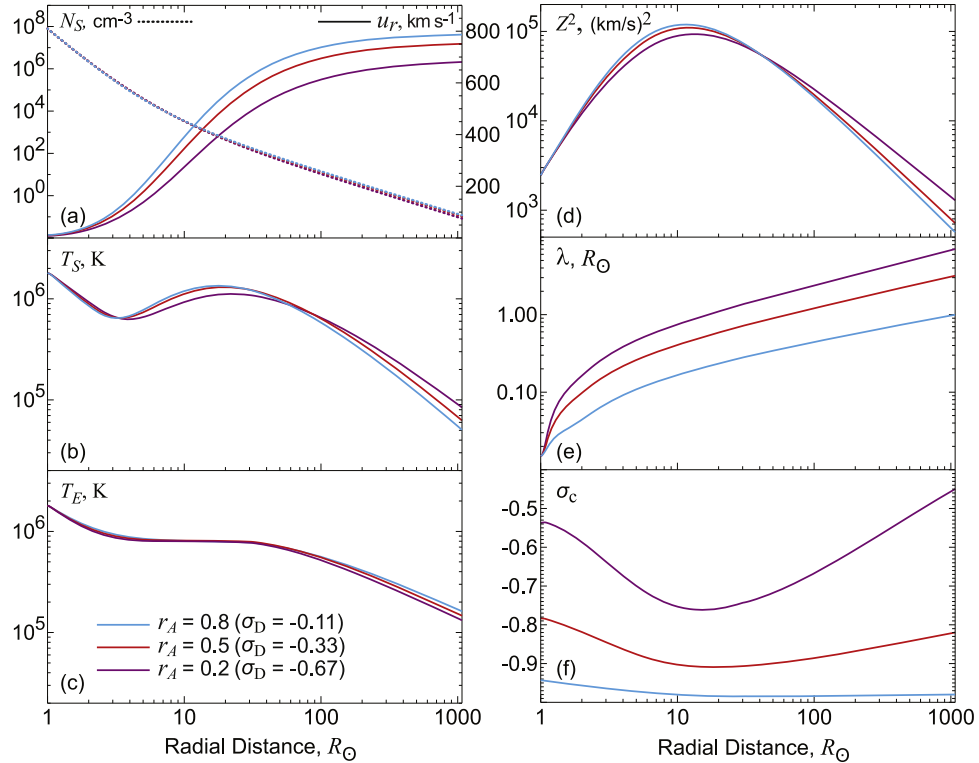


Figure 9. Same as in Figure 6, but for various values of the Alfvén ratio $r_A = (1 + \sigma_D)/(1 - \sigma_D)$.

distribution on the inner boundary and reveals the opposite behavior. At 0.3 au, it is larger in slow wind and decreases toward the fast wind.

We have derived a formula for the angular momentum loss due to outflowing plasma taking into account effects of turbulence. The

simulation results show that the angular momentum loss of the Sun can be notably affected by turbulence effects. We plan further study of this influence, which may be broadly of interest in astrophysics. The upcoming *Parker Solar Probe* mission will also afford an opportunity for additional observational constraints on

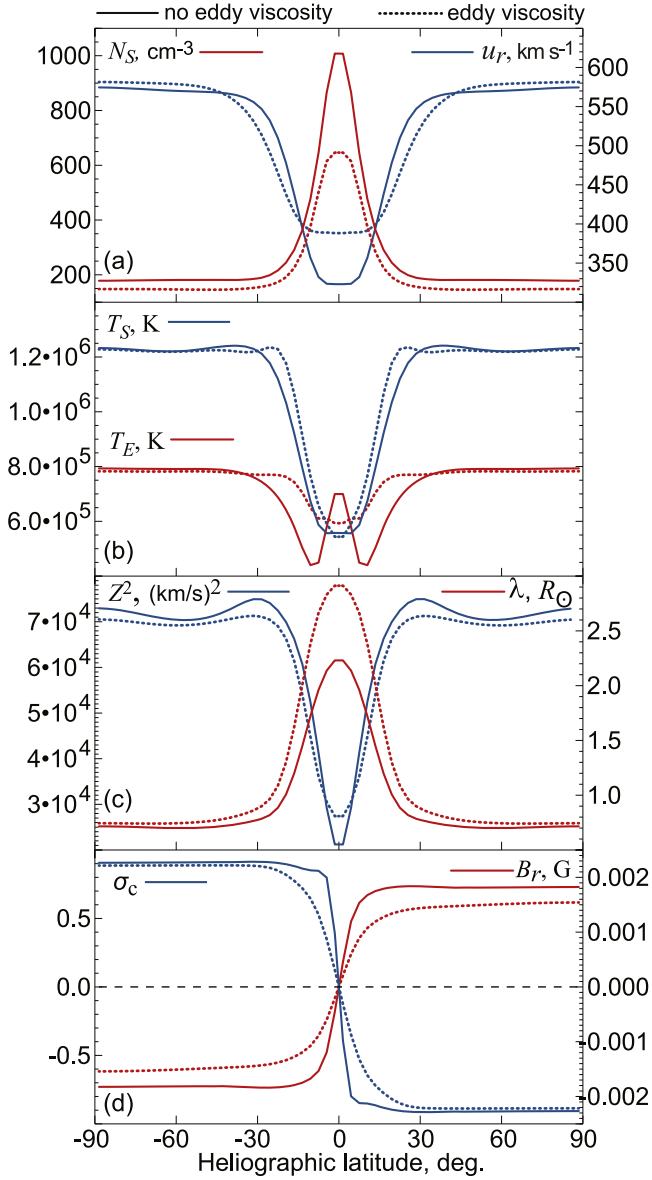


Figure 10. Latitudinal profiles at $30 R_{\odot}$ of the simulated (a) radial velocity u_r and proton density N_S , (b) proton T_S and electron T_E temperatures, (c) turbulence energy Z^2 and correlation scale λ , and (d) cross helicity σ_c and radial magnetic field B_r . The dotted (solid) lines depict the simulation results with the eddy viscosity turned on (off). The solar magnetic field is assumed to be an untitled dipole.

the azimuthal velocity and its implications for angular momentum loss rate of the Sun.

Following Breech et al. (2008, 2009), we continue to treat the normalized energy difference σ_D and the fraction of turbulent energy absorbed by protons f_p as constant parameters. The $\sigma_D = \text{const}$ approximation greatly simplifies equations, but it is based mostly on the fact that the observed ratio of kinetic to magnetic energy in fluctuations (the Alfvén ratio r_A) in the solar wind is often of order 0.5 with the corresponding value of $\sigma_D = -1/3$. An evolution equation for σ_D (see, e.g., Zhou & Matthaeus 1990; Tu & Marsch 1993; Yokoi et al. 2008; Zank et al. 2012, 2017) would be a useful improvement to the model, but since σ_D is not a “cascaded” quantity, its modeling, especially its nonlinear modeling, poses difficulties (Grappin et al. 1983; Matthaeus et al. 1994; Hossain et al. 1995). The f_p factor is

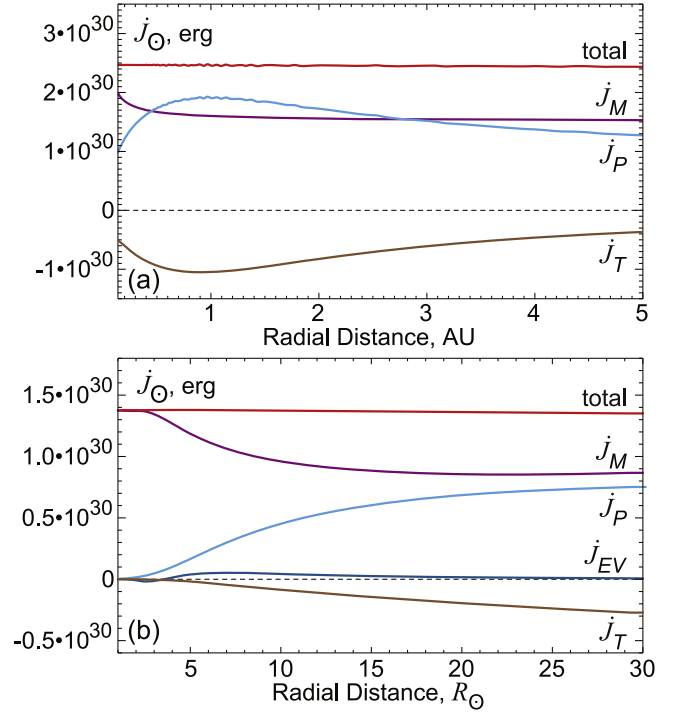


Figure 11. Radial profiles of the torque integral J_O (Equation (33)) and its components (a) in the outer region ($30 R_{\odot}$ –5 au) from the run without eddy viscosity and (b) in the inner region (1 – $30 R_{\odot}$) with the eddy viscosity turned on. The components of the torque integral are the plasma torque $J_p = \int_0^\pi \int_0^{2\pi} r^3 \sin^2 \theta \rho u_r u_\phi d\theta d\phi$, the magnetic torque $J_M = -\int_0^\pi \int_0^{2\pi} r^3 \sin^2 \theta (B_r B_\phi / 4\pi) d\theta d\phi$, the turbulent torque $J_T = -\int_0^\pi \int_0^{2\pi} r^3 \sin^2 \theta (\eta B_r B_\phi / 4\pi) d\theta d\phi$, and the eddy viscosity torque $J_{EV} = -\int_0^\pi \int_0^{2\pi} r^3 \sin^2 \theta \rho (\nu_K S_{r\phi} + \nu_M M_{r\phi}) d\theta d\phi$.

another quantity that can depend on radial distance (Cranmer et al. 2009) and be a function of plasma parameters (Matthaeus et al. 2016). We leave these refinements for future work.

Equations (18)–(19) have been derived assuming that the turbulence is incompressible and fluctuations of density and thermal pressures are negligible. The observed fluctuations in the solar wind are indeed mostly incompressible (Belcher & Davis 1971; Matthaeus et al. 1990), but a weak compressible component is also present and should be included in the model. This is a limitation that will be addressed in future work.

We gratefully acknowledge Stuart Bale, Sean Oughton, Tulasi Parashar, and Debanjan Sengupta for valuable discussions. The *Ulysses* data used in this study were obtained from the NASA/GSFC’s Space Physics Data Facility’s OMNIWeb service at <http://omniweb.gsfc.nasa.gov>. This work was supported in part by NASA LWS program (grant NNX15AB88G), NASA Heliophysics Grand Challenges Research program (grant NNX14AI63G), NASA Heliophysics Supporting Research program (grant 80NSSC18K1210), and the *Parker Solar Probe* project through the IS \odot IS theory team and subcontract SUB0000165 from Princeton University. Computing resources supporting this work were provided by the NASA High-End Computing (HEC) Program awards SMD-16-6890 and SMD-16-7606 through the NASA Advanced Supercomputing (NAS) Division at the Ames Research Center and the NASA Center for Climate Simulation (NCCS) at the Goddard Space Flight Center.

Appendix A Angular Momentum Loss in a Three-dimensional Geometry

We start from the momentum Equation (10). For simplicity, we first neglect turbulence effects by dropping the \mathcal{R} and $\langle B'^2 \rangle / 8\pi$ terms and avoid splitting of the magnetic field into the potential and nonpotential parts ($\mathbf{B}_1 = \mathbf{B}$ and $\mathbf{B}_0 = 0$). Then, Equation (10) takes the form

$$\begin{aligned} \frac{\partial(\rho\mathbf{u})}{\partial t} + \nabla \cdot \left(\rho\mathbf{v}\mathbf{u} + P_T\mathbf{I} - \frac{\mathbf{B}\mathbf{B}}{4\pi} \right) \\ + \rho \left(\frac{GM_\odot}{r^2} \hat{\mathbf{r}} + \boldsymbol{\Omega} \times \mathbf{u} \right) = 0, \end{aligned} \quad (39)$$

where $P_T = P_S + P_E + B^2/8\pi$. In the spherical coordinates (r, θ, ϕ) with the polar axis directed along the solar rotation axis, $v_\phi = u_\phi - \Omega r \sin \theta$ and the azimuthal component of Equation (39) is

$$\begin{aligned} \frac{\partial}{\partial t}(\rho u_\phi) = & -\frac{1}{r^2} \frac{\partial}{\partial r} \left[r^2 \left(\rho u_r u_\phi - \frac{B_r B_\phi}{4\pi} \right) \right] \\ & - \frac{1}{r \sin \theta} \frac{\partial}{\partial \theta} \left[\sin \theta \left(\rho u_\theta u_\phi - \frac{B_\theta B_\phi}{4\pi} \right) \right] \\ & - \frac{1}{r \sin \theta} \frac{\partial}{\partial \phi} \left(\rho u_\phi v_\phi + P_T - \frac{B_\phi^2}{4\pi} \right) \\ & - \frac{1}{r} \left[\rho u_r u_\phi - \frac{B_r B_\phi}{4\pi} + \cot \theta \left(\rho u_\theta u_\phi - \frac{B_\theta B_\phi}{4\pi} \right) \right]. \end{aligned} \quad (40)$$

In a steady state, Equation (40) takes the form (see Pizzo 1982, Equation (15))

$$\begin{aligned} \frac{1}{r^3} \frac{\partial}{\partial r} \left[r^3 \left(\rho u_r u_\phi - \frac{B_r B_\phi}{4\pi} \right) \right] \\ = -\frac{1}{r \sin \theta} \frac{\partial}{\partial \theta} \left[\sin \theta \left(\rho u_\theta u_\phi - \frac{B_\theta B_\phi}{4\pi} \right) \right] \\ - \frac{1}{r \sin \theta} \frac{\partial}{\partial \phi} \left(\rho u_\phi v_\phi + P_T - \frac{B_\phi^2}{4\pi} \right) \\ - \frac{\cot \theta}{r} \left(\rho u_\theta u_\phi - \frac{B_\theta B_\phi}{4\pi} \right). \end{aligned} \quad (41)$$

Multiplying Equation (41) by $r \sin \theta$, i.e., rewriting it in terms of a torque balance along the direction of the rotation axis, and integrating over a sphere of radius r , we have

$$\begin{aligned} \int_0^\pi \int_0^{2\pi} \frac{\partial}{\partial r} \left[r^3 \sin^2 \theta \left(\rho u_r u_\phi - \frac{B_r B_\phi}{4\pi} \right) \right] d\theta d\phi \\ = - \int_0^\pi \int_0^{2\pi} r^2 \sin \theta \frac{\partial}{\partial \theta} \left[\sin \theta \left(\rho u_\theta u_\phi - \frac{B_\theta B_\phi}{4\pi} \right) \right] d\theta d\phi \\ - \int_0^\pi \int_0^{2\pi} \frac{\partial}{\partial \phi} \left[r^2 \sin \theta \left(\rho u_\phi v_\phi + P_T - \frac{B_\phi^2}{4\pi} \right) \right] d\theta d\phi \\ - \int_0^\pi \int_0^{2\pi} r^2 \sin \theta \cos \theta \left(\rho u_\theta u_\phi - \frac{B_\theta B_\phi}{4\pi} \right) d\theta d\phi. \end{aligned} \quad (42)$$

By integrating the first term on the right-hand side over θ by parts, it is easy to show that it is equal to the third integral with the opposite sign, and therefore they cancel. The second integral on the right-hand side also disappears after integration over a period in ϕ . Therefore, we have

$$\frac{\partial}{\partial r} \int_0^\pi \int_0^{2\pi} r^3 \sin^2 \theta \left(\rho u_r u_\phi - \frac{B_r B_\phi}{4\pi} \right) d\theta d\phi = 0. \quad (43)$$

The integral in Equation (43) is the torque applied to the Sun by the outflowing magnetized plasma of the solar wind. Obviously, it can be computed over a sphere of any radius.

If we do not neglect turbulence effects but still set $\mathbf{B}_1 = \mathbf{B}$ and $\mathbf{B}_0 = 0$, the azimuthal component of the momentum Equation (10) can be rewritten in a steady state as

$$\begin{aligned} \frac{1}{r^3} \frac{\partial}{\partial r} \left[r^3 \left(\rho u_r u_\phi - \frac{B_r B_\phi}{4\pi} + \mathcal{R}_{r\phi} \right) \right] \\ = -\frac{1}{r \sin \theta} \frac{\partial}{\partial \theta} \left[\sin \theta \left(\rho u_\theta u_\phi - \frac{B_\theta B_\phi}{4\pi} + \mathcal{R}_{\theta\phi} \right) \right] \\ - \frac{1}{r \sin \theta} \frac{\partial}{\partial \phi} \left(\rho u_\phi v_\phi + P_T - \frac{B_\phi^2}{4\pi} + \mathcal{R}_{\phi\phi} \right) \\ - \frac{\cot \theta}{r} \left(\rho u_\theta u_\phi - \frac{B_\theta B_\phi}{4\pi} + \mathcal{R}_{\theta\phi} \right), \end{aligned} \quad (44)$$

where \mathcal{R}_{ij} are the spherical components of the Reynolds stress tensor and the total pressure $P_T = P_S + P_E + (1 - \sigma_D) \rho Z^2/4$ now includes a contribution from turbulence. Integration of Equation (44) over a sphere of arbitrary radius r gives the similar result

$$\begin{aligned} J = \int_0^\pi \int_0^{2\pi} r^3 \sin^2 \theta \left(\rho u_r u_\phi - \frac{B_r B_\phi}{4\pi} + \mathcal{R}_{r\phi} \right) d\theta d\phi \\ = \text{const}, \end{aligned} \quad (45)$$

where the $\mathcal{R}_{r\phi}$ component of the Reynolds stress tensor now appears in the integral. Equation (45) shows that turbulence affects the loss of angular momentum of the Sun and other stars if $\mathcal{R}_{r\phi} \neq 0$. The integral in Equation (43) coincides with the torque formula in Vidotto et al. (2014, see their Appendix A). In addition, our derivation proves that the integral over a sphere is independent of its radius. Note that the formula for the angular momentum loss used in a number of three-dimensional studies (e.g., Strugarek et al. 2014; Réville et al. 2016; Pantolmos & Matt 2017) is identical to the integral in Equation (43) only if $u_\theta = 0$ and $B_\theta = 0$.

Appendix B The System of Governing Equations in Nondimensional Form on a Logarithmic Grid

To rewrite the governing system of equations in nondimensional form, we define the following nondimensional parameters: the Strouhal number $S_h = u_0 t_0 / L_0$, the Euler number $E_u = P_0 / \rho_0 u_0^2$, the Froude number $F_r = u_0^2 L_0 / GM_\odot$, and the Alfvén Mach number $M_A = u_0 (4\pi \rho_0)^{1/2} / B_0$. $L_0, t_0, \rho_0, u_0, B_0$, and P_0 are units of length, time, density, velocity, magnetic field, and thermal pressure, respectively. Using the logarithmic transformation of the radial coordinate r to a new one $r' = \ln(r/r_0)$, where $r_0 = 1 R_\odot$, we can rewrite the composite set of Equations (1)

(4)–(5), (10)–(11), and (18)–(20) in spherical coordinates in the following dimensionless quasi-conservative form:

$$\frac{\partial \mathbf{W}}{\partial t} = \frac{\partial \mathbf{F}}{\partial r'} + \frac{\partial \mathbf{G}}{\partial \theta} + \frac{\partial \mathbf{H}}{\partial \phi} + \mathbf{S}, \quad (46)$$

where

$$\mathbf{W} = \begin{pmatrix} r^3 \rho \\ r^3 \rho u_r \\ r^3 \rho u_\theta \\ r^3 \rho u_\phi \\ r^2 B_{1r} \\ r^2 B_{1\theta} \\ r^2 B_{1\phi} \\ r^3 P_S \\ r^3 Z^2 \\ r^3 Z^2 \sigma_c \\ r^3 \rho \lambda \\ r^3 P_E \end{pmatrix}, \quad \mathbf{F} = -S_h \begin{pmatrix} r^2 \rho u_r \\ r^2 \left(\rho u_r^2 + P_T - \frac{B_{1r} B_r^*}{M_A^2} + \mathcal{R}_{rr} \right) \\ r^2 \left(\rho u_r u_\theta - \frac{B_{1r} B_\theta + B_{0r} B_{1\theta}}{M_A^2} + \mathcal{R}_{r\theta} \right) \\ r^2 \left(\rho u_r u_\phi - \frac{B_{1r} B_\phi + B_{0r} B_{1\phi}}{M_A^2} + \mathcal{R}_{r\phi} \right) \\ 0 \\ r(u_r B_\theta - v_\theta B_r + \varepsilon_{m\phi} M_A \sqrt{\rho}) \\ -r(v_\phi B_r - u_r B_\phi + \varepsilon_{m\theta} M_A \sqrt{\rho}) \\ r^2 u_r P_S \\ r^2 Z^2 (u_r - \sigma_c V_{Ar}) \\ r^2 Z^2 (\sigma_c u_r - V_{Ar}) \\ r^2 u_r \rho \lambda \\ r^2 [u_r P_E + (\gamma - 1) q_{Er}] \end{pmatrix},$$

$$\mathbf{G} = -S_h \begin{pmatrix} r^2 \rho v_\theta \\ r^2 \left(\rho u_r v_\theta - \frac{B_{1r} B_\theta + B_{0r} B_{1\theta}}{M_A^2} + \mathcal{R}_{r\theta} \right) \\ r^2 \left(\rho u_\theta v_\theta + P_T - \frac{B_{1\theta} B_\theta^*}{M_A^2} + \mathcal{R}_{\theta\theta} \right) \\ r^2 \left(\rho v_\theta u_\phi - \frac{B_{1\theta} B_\phi + B_{0\theta} B_{1\phi}}{M_A^2} + \mathcal{R}_{\theta\phi} \right) \\ -r(u_r B_\theta - v_\theta B_r + \varepsilon_{m\phi} M_A \sqrt{\rho}) \\ 0 \\ r(v_\theta B_\phi - v_\phi B_\theta + \varepsilon_{mr} M_A \sqrt{\rho}) \\ r^2 v_\theta P_S \\ r^2 Z^2 (v_\theta - \sigma_c V_{A\theta}) \\ r^2 Z^2 (\sigma_c v_\theta - V_{A\theta}) \\ r^2 v_\theta \rho \lambda \\ r^2 [v_\theta P_E + (\gamma - 1) q_{E\theta}] \end{pmatrix},$$

$$\mathbf{H} = -\frac{S_h}{\sin \theta} \begin{pmatrix} r^2 \rho v_\phi \\ r^2 \left(\rho u_r v_\phi - \frac{B_{1r} B_\phi + B_{0r} B_{1\phi}}{M_A^2} + \mathcal{R}_{r\phi} \right) \\ r^2 \left(\rho u_\theta v_\phi - \frac{B_{1\theta} B_\phi + B_{0\theta} B_{1\phi}}{M_A^2} + \mathcal{R}_{\theta\phi} \right) \\ r^2 \left(\rho u_\phi v_\phi + P_T - \frac{B_{1\phi} B_\phi^*}{M_A^2} + \mathcal{R}_{\phi\phi} \right) \\ r(v_\phi B_r - u_r B_\phi + \varepsilon_{m\theta} M_A \sqrt{\rho}) \\ -r(v_\theta B_\phi - v_\phi B_\theta + \varepsilon_{mr} M_A \sqrt{\rho}) \\ 0 \\ r^2 v_\phi P_S \\ r^2 Z^2 (v_\phi - \sigma_c V_{A\phi}) \\ r^2 Z^2 (\sigma_c v_\phi - V_{A\phi}) \\ r^2 v_\phi \rho \lambda \\ r^2 [v_\phi P_E + (\gamma - 1) q_{E\phi}] \end{pmatrix},$$

$$\begin{aligned}
& \left(-r^2 \rho v_\theta \cot \theta \right. \\
& r^2 \rho \left[u_\theta^2 + u_\phi^2 - \frac{1}{F_r r} + \frac{2P_T}{\rho} - \frac{B_{1\theta} B_\theta^* + B_{1\phi} B_\phi^*}{M_A^2 \rho} + \frac{\mathcal{R}_{\theta\theta} + \mathcal{R}_{\phi\phi}}{\rho} - \cot \theta (u_r v_\theta \right. \\
& \left. \left. - \frac{B_{1r} B_\theta + B_{0r} B_{1\theta}}{M_A^2 \rho} + \frac{\mathcal{R}_{r\theta}}{\rho} \right) \right] - \frac{r^3 (B_{1r} \nabla \cdot \mathbf{B} + B_{0r} \nabla \cdot \mathbf{B}_1)}{M_A^2} \\
& - r^2 \rho \left[u_r u_\theta - \frac{B_{1r} B_\theta + B_{0r} B_{1\theta}}{M_A^2 \rho} + \frac{\mathcal{R}_{r\theta}}{\rho} + \cot \theta \left(u_\theta v_\theta - u_\phi^2 + \frac{\mathcal{R}_{\theta\theta} - \mathcal{R}_{\phi\phi}}{\rho} \right. \right. \\
& \left. \left. - \frac{B_{1\theta} B_\theta^* - B_{1\phi} B_\phi^*}{M_A^2 \rho} \right) + u_\phi \mu \right] - \frac{r^3 (B_{1\theta} \nabla \cdot \mathbf{B} + B_{0\theta} \nabla \cdot \mathbf{B}_1)}{M_A^2} \\
& - r^2 \rho \left\{ u_r u_\phi - \frac{B_{1r} B_\phi + B_{0r} B_{1\phi}}{M_A^2 \rho} + \frac{\mathcal{R}_{r\phi}}{\rho} + \cot \theta \left[(u_\theta + v_\theta) u_\phi + \frac{2\mathcal{R}_{\theta\phi}}{\rho} \right. \right. \\
& \left. \left. - \frac{2(B_{1\theta} B_\phi + B_{0\theta} B_{1\phi})}{M_A^2 \rho} \right] - u_\theta \mu \right\} - \frac{r^3 (B_{1\phi} \nabla \cdot \mathbf{B} + B_{0\phi} \nabla \cdot \mathbf{B}_1)}{M_A^2} \\
& r \cot \theta (u_r B_\theta - v_\theta B_r + \varepsilon_{m\phi} M_A \sqrt{\rho}) - r^2 u_r \nabla \cdot \mathbf{B} \\
& - r^2 v_\theta \nabla \cdot \mathbf{B} \\
& S = S_h - r^2 v_\phi \nabla \cdot \mathbf{B} \\
& - r^2 \left\{ v_\theta P_S \cot \theta - r(\gamma - 1) \left[-P_S \nabla \cdot \mathbf{u} + \frac{P_E - P_S}{\tau_{SE} S_h} + f_p \frac{\alpha f^+(\sigma_c) \rho Z^3}{2\lambda E_u} \right] \right\} \\
& - r^2 \left\{ Z^2 (v_\theta - \sigma_c V_{A\theta}) \cot \theta - r \left[\frac{Z^2}{2} ((1 + \sigma_D) \nabla \cdot \mathbf{u} - 4\sigma_c \nabla \cdot \mathbf{V}_A) \right. \right. \\
& \left. \left. - \frac{2}{\rho} \mathcal{R} : \nabla \mathbf{u} - 2\varepsilon_m \cdot (\nabla \times \mathbf{V}_A) - \frac{\alpha f^+(\sigma_c) Z^3}{\lambda} + \frac{Z^2 \sigma_c \nabla \cdot \mathbf{B}}{M_A \sqrt{\rho}} \right] \right\} \\
& - r^2 \left\{ Z^2 (\sigma_c v_\theta - V_{A\theta}) \cot \theta - r \left[\frac{Z^2}{2} (\sigma_c \nabla \cdot \mathbf{u} + 2(\sigma_D - 2) \nabla \cdot \mathbf{V}_A) \right. \right. \\
& \left. \left. - \frac{2}{\rho} \mathcal{R} : \nabla \mathbf{V}_A - 2\varepsilon_m \cdot (\nabla \times \mathbf{u}) - \frac{\alpha f^-(\sigma_c) Z^3}{\lambda} + \frac{(1 - \sigma_D) Z^2 \nabla \cdot \mathbf{B}}{M_A \sqrt{\rho}} \right] \right\} \\
& - r^2 \rho [\lambda v_\theta \cot \theta - r \beta f^+(\sigma_c) Z] \\
& - r^2 \left\{ [v_\theta P_E + (\gamma - 1) q_{E\theta}] \cot \theta - r(\gamma - 1) \left[-P_E \nabla \cdot \mathbf{u} + \frac{P_S - P_E}{\tau_{SE} S_h} \right. \right. \\
& \left. \left. + (1 - f_p) \frac{\alpha f^+(\sigma_c) \rho Z^3}{2\lambda E_u} - N_E^2 \Phi'(T_E) \right] \right\}
\end{aligned}
\right),$$

and all the physical quantities are normalized to their respective units. In particular, the nondimensional Alfvén velocity components are $V_{Ar,\theta,\phi} = B_{r,\theta,\phi}/M_A \sqrt{\rho}$, and the total pressure is

$$\begin{aligned}
P_T = (P_S + P_E) E_u + \frac{B_{r1} B_r^* + B_{\theta1} B_\theta^* + B_{\phi1} B_\phi^*}{2M_A^2} \\
+ \frac{(1 - \sigma_D) \rho Z^2}{4}.
\end{aligned} \quad (47)$$

Other notations: $B_{r,\theta,\phi}^* = B_{1r,\theta,\phi} + 2B_{0r,\theta,\phi}$, and $\Phi'(T_E) = (\rho_0^2 L_0 / m_p^2 u_0 P_0) \Phi(T_E)$ is the nondimensional radiation loss function. The function

$$\mu = \frac{R_o r \sin \phi}{\sin \theta} \quad (48)$$

emerges in the source terms of tangential momentum equations only for the two polar fragments of the composite spherical grid (Usmanov et al. 2012) as a result of solar rotation. It is identically equal to zero for the main spherical fragment. The

dimensionless electron heat flux is $q'_E = \psi q'_H + (1 - \psi) q'_S$, where

$$q'_S = - \frac{\kappa_0 P_0^{7/2}}{u_0 P_0 L_0 (k_B N_0)^{7/2}} \left(\frac{P_E}{N_E} \right)^{5/2} \hat{\mathbf{B}} (\hat{\mathbf{B}} \cdot \nabla) \left(\frac{P_E}{N_E} \right), \quad (49)$$

$q'_H = \alpha_H P_E v$, and ψ is defined by Equation (17).

In the outer region we do not separate the magnetic field into the internal (potential) \mathbf{B}_0 and nonpotential \mathbf{B}_1 components (see Section 2.1), so the equations in the outer region are the same as above with $\mathbf{B}_0 = 0$ and $\mathbf{B}_1 = \mathbf{B}$. Note that Equation (46) does not assume that the magnetic field is divergence-free, and in addition to the standard terms of Powell et al. (1999) in the momentum and induction equations, the appropriate $\nabla \cdot \mathbf{B}$ -terms appear also in the equations for turbulence energy and cross helicity.

ORCID iDs

Arcadi V. Usmanov  <https://orcid.org/0000-0002-0209-152X>

William H. Matthaeus  <https://orcid.org/0000-0001-7224-6024>

Melvyn L. Goldstein  <https://orcid.org/0000-0002-5317-988X>

Rohit Chhiber  <https://orcid.org/0000-0002-7174-6948>

References

- Agarwal, R. K., & Deese, J. E. 1987, *JAir*, 24, 231
- Altschuler, M. D., & Newkirk, G. A. 1969, *SoPh*, 9, 131
- Arge, C. N., Odstrčil, D., Pizzo, V. J., & Mayer, L. R. 2003, in AIP Conf. Proc. 679, Solar Wind 10, ed. M. Velli, R. Bruno, & F. Malara (Melville, NY: AIP), 190
- Barnes, A., Gazis, P. R., & Phillips, J. L. 1995, *GeoRL*, 22, 3309
- Belcher, J. W. 1971, *ApJ*, 168, 509
- Belcher, J. W., & Davis, L. 1971, *JGR*, 76, 3534
- Biskamp, D. 2003, *Magnetohydrodynamic Turbulence* (Cambridge: Cambridge Univ. Press)
- Breech, B., Matthaeus, W. H., Cranmer, S. R., Kasper, J. C., & Oughton, S. 2009, *JGR*, 114, A09103
- Breech, B., Matthaeus, W. H., Minnie, J., et al. 2008, *JGR*, 113, A08105
- Bretherton, F. P. 1971, in *Mathematical Problems in the Geophysical Sciences* Vol. 1, ed. W. H. Reid (Providence, RI: American Mathematical Society), 61
- Chandran, B. D. G., Dennis, T. J., Quataert, E., & Bale, S. D. 2011, *ApJ*, 743, 197
- Chen, Y., & Hu, Y. Q. 2001, *SoPh*, 199, 371
- Chhiber, R., Subedi, P., Usmanov, A. V., et al. 2017, *ApJS*, 230, 21
- Chhiber, R., Usmanov, A. V., DeForest, C. E., et al. 2018a, *ApJL*, 856, L39
- Chhiber, R., Usmanov, A. V., Matthaeus, W. H., & Goldstein, M. L. 2016, *ApJ*, 821, 34
- Chhiber, R., Usmanov, A. V., Matthaeus, W. H., & Goldstein, M. L. 2018b, *ApJS*, submitted (arXiv:1806.00570)
- Cohen, O., Sokolov, I. V., Roussev, I. I., et al. 2007, *ApJL*, 654, L163
- Cranmer, S. R., Matthaeus, W. H., Breech, B. A., & Kasper, J. C. 2009, *ApJ*, 702, 1604
- Cranmer, S. R., & van Ballegoijen, A. A. 2012, *ApJ*, 754, 92
- de Kármán, T., & Howarth, L. 1938, *RSPSA*, 164, 192
- Detman, T. R., Intriligator, D. S., Dryer, M., et al. 2011, *JGR*, 116, A03105
- Detman, T. R., Smith, Z. K., Dryer, M., et al. 2006, *JGR*, 111, A07102
- Dewar, R. L. 1970, *PhFl*, 13, 2710
- Dmitruk, P., Matthaeus, W. H., Milano, L. J., et al. 2002, *ApJ*, 575, 571
- Dmitruk, P., Milano, L. J., & Matthaeus, W. H. 2001, *ApJ*, 548, 482
- Dryden, H. L. 1943, *QApMa*, 1, 7
- Einfeldt, B., Munz, C. D., Roe, P. L., & Sjögreen, B. 1991, *JCoPh*, 92, 273
- Endler, F. 1971, PhD thesis, Max-Planck-Institut für Physik und Astrophysik
- Esser, R., Leer, E., Habbal, S. R., & Withbroe, G. L. 1986, *JGR*, 91, 2950
- Feng, X., Yang, L., Xiang, C. Q., et al. 2010, *ApJ*, 723, 300
- Feng, X., Zhang, M., & Zhou, Y. 2014, *ApJS*, 214, 6
- Gosling, J. T., & Pizzo, V. J. 1999, *SSRv*, 89, 21
- Gottlieb, S., Shu, C.-W., & Tadmor, E. 2001, *SIAMR*, 43, 89
- Grappin, R., Pouquet, A., & L  orat, J. 1983, *A&A*, 126, 51
- Groth, C. P. T., De Zeeuw, D. L., Gombosi, T. I., & Powell, K. G. 2000, *JGR*, 105, 25053
- Habbal, S. R., Hu, Y. Q., & Esser, R. 1994, *JGR*, 99, 8465
- Hartle, R. E., & Barnes, A. 1970, *JGR*, 75, 6915
- Hartle, R. E., & Sturrock, P. A. 1968, *ApJ*, 151, 1155
- Hayashi, K. 2005, *ApJS*, 161, 480
- Hollweg, J. V. 1974, *JGR*, 79, 3845
- Hollweg, J. V. 1976, *JGR*, 81, 1649
- Hollweg, J. V. 1978, *RvGSP*, 16, 689
- Hollweg, J. V. 1990, *CoPhR*, 12, 205
- Hossain, M., Gray, P. C., Pontius, D. H., Matthaeus, W. H., & Oughton, S. 1995, *PhFl*, 7, 2886
- Hu, X. Y., & Khoo, B. C. 2003, *JCoPh*, 193, 243
- Hu, Y. Q., Li, X., & Habbal, S. R. 2003, *JGR*, 108, 1378
- Hu, Y. Q., & Wu, S. T. 1984, *JCoPh*, 55, 33
- Hundhausen, A. J. 1972, *Coronal Expansion and Solar Wind* (Berlin: Springer)
- Isenberg, P. A., Smith, C. W., & Matthaeus, W. H. 2003, *ApJ*, 592, 564
- Jacques, S. A. 1978, *ApJ*, 226, 632
- Kryukov, I. A., Pogorelov, N. V., Zank, G. P., & Borovikov, S. N. 2012, in AIP Conf. Proc. 1436, Physics of the Heliosphere: A 10 Year Retrospective: Proc. X Annual International Astrophysics Conf., ed. J. Heerikhuisen et al. (Melville, NY: AIP), 48
- Kurganov, A., & Levy, D. 2000, *SIAM J. Sci. Comput.*, 22, 1461
- L  v  que, E., Toschi, F., Shao, L., & Bertoglio, J.-P. 2007, *JFM*, 570, 491
- Levine, R. H., Altschuler, M. D., & Harvey, J. W. 1977, *JGR*, 82, 1061
- Li, B., Li, X., Hu, Y. Q., & Habbal, S. R. 2004, *JGR*, 109, A07103
- Linker, J. A., Van Hoven, G., & Schnack, D. D. 1990, *GeoRL*, 17, 2281
- Lionello, R., Linker, J. A., & Miki  , Z. 2001, *ApJ*, 546, 542
- Lionello, R., Linker, J. A., & Miki  , Z. 2009, *ApJ*, 690, 902
- Lionello, R., Velli, M., Downs, C., et al. 2014a, *ApJ*, 784, 120
- Lionello, R., Velli, M., Downs, C., Linker, J. A., & Miki  , Z. 2014b, *ApJ*, 796, 111
- Lyon, J. G., Fedder, J. A., & Mobarri, C. M. 2004, *JATP*, 66, 1333
- Marsch, E., & Tu, C. Y. 1992, in *Solar Wind Seven*, Proc. 3rd COSPAR Coll., ed. E. Marsch & R. Schwenn (Oxford: Pergamon), 505
- Matthaeus, W. H., & Goldstein, M. L. 1982, *JGR*, 87, 6011
- Matthaeus, W. H., Goldstein, M. L., & Roberts, D. A. 1990, *JGR*, 95, 20673
- Matthaeus, W. H., Minnie, J., Breech, B., et al. 2004, *GeoRL*, 31, L12803
- Matthaeus, W. H., Oughton, S., Pontius, D. H., & Zhou, Y. 1994, *JGR*, 99, 19267
- Matthaeus, W. H., Parashar, T. N., Wan, M., & Wu, P. 2016, *ApJL*, 827, L7
- Matthaeus, W. H., & Velli, M. 2011, *SSRv*, 160, 145
- Matthaeus, W. H., Zank, G. P., & Oughton, S. 1996, *JPhPh*, 56, 659
- Matthaeus, W. H., Zank, G. P., Oughton, S., Mullan, D. J., & Dmitruk, P. 1999a, *ApJL*, 523, L93
- Matthaeus, W. H., Zank, G. P., Smith, C. W., & Oughton, S. 1999b, *PhRvL*, 82, 3444
- Merkin, V. G., Lyon, J. G., Lario, D., Arge, C. N., & Henney, C. J. 2016, *JGR*, 121, 2866
- Munro, R. H., & Jackson, B. V. 1977, *ApJ*, 213, 874
- Nakagawa, Y., & Steinolfson, R. S. 1976, *ApJ*, 207, 296
- Nakamizo, A., Tanaka, T., Kubo, Y., et al. 2009, *JGR*, 114, A07109
- Odstr  il, D. 2003, *AdSpR*, 32, 497
- Pantolmos, G., & Matt, S. P. 2017, *ApJ*, 849, 83
- Parker, E. N. 1958, *ApJ*, 128, 664
- Pizzo, V. J. 1978, *JGR*, 83, 5563
- Pizzo, V. J. 1982, *JGR*, 87, 4374
- Pneuman, G. W., & Kopp, R. A. 1971, *SoPh*, 18, 258
- Podesta, J. J., Roberts, D. A., & Goldstein, M. L. 2007, *ApJ*, 664, 543
- Pogorelov, N. V., Bedford, M. C., Kryukov, I. A., & Zank, G. P. 2016, *JPhCS*, 767, 012020
- Pogorelov, N. V., Borovikov, S. N., Kryukov, I. A., et al. 2017a, *JPhCS*, 837, 012014
- Pogorelov, N. V., Fichtner, H., Czechowski, A., et al. 2017b, *SSRv*, 212, 193
- Powell, K. G., Roe, P. L., Linde, T. J., Gombosi, T. I., & De Zeeuw, D. L. 1999, *JCoPh*, 154, 284
- Priest, E. R. 1982, *Solar Magnetohydrodynamics* (Dordrecht: Reidel)
- Raeder, J. 2003, in *Space Plasma Simulation* Vol. 615, ed. J. B  chner, C. T. Dum, & M. Scholer (Berlin: Springer), 212
- R  ville, V., Folsom, C. P., Strugarek, A., & Brun, A. S. 2016, *ApJ*, 832, 145
- Riley, P., Ben-Nun, M., Linker, J. A., et al. 2014, *SoPh*, 289, 769
- Riley, P., Linker, J. A., Lionello, R., & Miki  , Z. 2012, *JATP*, 83, 1
- Riley, P., Linker, J. A., & Miki  , Z. 2001, *JGR*, 106, 15889
- Schatten, K. H., Wilcox, J. M., & Ness, N. F. 1969, *SoPh*, 6, 442
- Scudder, J. D., & Olbert, S. 1979, *JGR*, 84, 2755
- Shiota, D., Kataoka, R., Miyoshi, Y., et al. 2014, *SpWea*, 12, 187
- Shiota, D., Zank, G. P., Adhikari, L., et al. 2017, *ApJ*, 837, 75
- Smith, C. W., Matthaeus, W. H., Zank, G. P., et al. 2001, *JGR*, 106, 8253

- Sokolov, I. V., van der Holst, B., Oran, R., et al. 2013, *ApJ*, **764**, 23
- Spitzer, L. 1962, *Physics of Fully Ionized Gases* (New York: Interscience)
- Steinolfson, R. S., & Nakagawa, Y. 1976, *ApJ*, **207**, 300
- Steinolfson, R. S., Suess, S. T., & Wu, S. T. 1982, *ApJ*, **255**, 730
- Strugarek, A., Brun, A. S., Matt, S. P., & Réville, V. 2014, arXiv:1410.3537
- Svalgaard, L. 2006, Presentation at 2006 SHINE Workshop, http://www.shinecon.org/Presentations/2006/WG2/LS/Svalgaard-talk_SHINE_06.pdf
- Svalgaard, L., Duvall, T. L., Jr., & Scherrer, P. H. 1978, *SoPh*, **58**, 225
- Tanaka, T. 1994, *JCoPh*, **111**, 381
- Thompson, K. W. 1990, *JCoPh*, **89**, 439
- Tóth, G., Sokolov, I. V., Gombosi, T. I., et al. 2005, *JGR*, **110**, A12226
- Tóth, G., van der Holst, B., Sokolov, I. V., et al. 2012, *JCoPh*, **231**, 870
- Tu, C.-Y., & Marsch, E. 1993, *JGR*, **98**, 1257
- Tu, C.-Y., & Marsch, E. 1995, *SSRv*, **73**, 1
- Ulrich, R. K. 1992, in ASP Conf. Ser. 26, Seventh Cambridge Workshop on Cool Stars, Stellar Systems, and the Sun, ed. M. S. Giampapa & J. A. Bookbinder (San Francisco, CA: ASP), 265
- Usmanov, A. V. 1993a, *SoPh*, **146**, 377
- Usmanov, A. V. 1993b, *SoPh*, **148**, 371
- Usmanov, A. V. 1996, in AIP Conf. Proc. 382, Solar Wind 8, ed. D. Winterhalter et al. (Melville, NY: AIP), 141
- Usmanov, A. V., & Dryer, M. 1995, *SoPh*, **159**, 347
- Usmanov, A. V., & Goldstein, M. L. 2003, *JGR*, **108**, 1354
- Usmanov, A. V., Goldstein, M. L., Besser, B. P., & Fritzer, J. M. 2000, *JGR*, **105**, 12675
- Usmanov, A. V., Goldstein, M. L., & Matthaeus, W. H. 2012, *ApJ*, **754**, 40
- Usmanov, A. V., Goldstein, M. L., & Matthaeus, W. H. 2014, *ApJ*, **788**, 43
- Usmanov, A. V., Goldstein, M. L., & Matthaeus, W. H. 2016, *ApJ*, **820**, 17
- Usmanov, A. V., Matthaeus, W. H., Breech, B., & Goldstein, M. L. 2009, in ASP Conf. Ser. 406, Numerical Modeling of Space Plasma Flows: ASTRONUM—2008, ed. N. V. Pogorelov et al. (San Francisco, CA: ASP), 160
- Usmanov, A. V., Matthaeus, W. H., Breech, B., & Goldstein, M. L. 2011, *ApJ*, **727**, 84
- van der Holst, B., Manchester, W. B., Frazin, R. A., et al. 2010, *ApJ*, **725**, 1373
- van der Holst, B., Sokolov, I. V., Meng, X., et al. 2014, *ApJ*, **782**, 81
- Verdini, A., Velli, M., Matthaeus, W. H., Oughton, S., & Dmitruk, P. 2010, *ApJL*, **708**, L116
- Vidotto, A. A., Jardine, M., Morin, J., et al. 2014, *MNRAS*, **438**, 1162
- Wang, A. H., Wu, S. T., Suess, S. T., & Poletto, G. 1998, *JGR*, **103**, 1913
- Wang, S., Hu, Y. Q., & Wu, S. T. 1982, *SciSn*, **25**, 1305
- Wang, Y., Boldyrev, S., & Perez, J. C. 2011, *ApJL*, **740**, L36
- Wang, Y.-M. 1993, *ApJL*, **410**, L123
- Wang, Y.-M., & Sheeley, N. R. 1990, *ApJ*, **355**, 726
- Wang, Y.-M., & Sheeley, N. R. 1992, *ApJ*, **392**, 310
- Wang, Y.-M., & Sheeley, N. R. 1997, *GeoRL*, **24**, 3141
- Weber, E. J., & Davis, L. 1970, *JGR*, **75**, 2419
- Wiengarten, T., Fichtner, H., Kleimann, J., & Kissmann, R. 2015, *ApJ*, **805**, 155
- Wiengarten, T., Kleimann, J., Fichtner, H., et al. 2013, *JGR*, **118**, 29
- Wiengarten, T., Kleimann, J., Fichtner, H., et al. 2014, *ApJ*, **788**, 80
- Wiengarten, T., Oughton, S., Engelbrecht, N. E., et al. 2016, *ApJ*, **833**, 17
- Withbroe, G. L. 1988, *ApJ*, **325**, 442
- Xia, Z., Shi, Y., & Zhao, Y. 2015, *JTurb*, **16**, 925
- Yalim, M. S., Pogorelov, N. V., & Liu, Y. 2017, *JPhCS*, **837**, 012015
- Yokoi, N. 2013, *GApFD*, **107**, 114
- Yokoi, N., Higashimori, K., & Hoshino, M. 2013, *PhPl*, **20**, 122310
- Yokoi, N., Rubinstein, R., Yoshizawa, A., & Hamba, F. 2008, *JTurb*, **9**, 1
- Yoshizawa, A. 1984, *PhFl*, **27**, 1377
- Yoshizawa, A. 1998, *Hydromagnetic and Magnetohydrodynamic Turbulent Flows: Modeling and Statistical Theory* (Dordrecht: Kluwer)
- Zank, G. P., Adhikari, L., Hunana, P., et al. 2017, *ApJ*, **835**, 147
- Zank, G. P., Dosch, A., Hunana, P., et al. 2012, *ApJ*, **745**, 35
- Zhao, X., & Hoeksema, J. T. 1995, *JGR*, **100**, 19
- Zhou, Y., & Matthaeus, W. H. 1990, *JGR*, **95**, 10291
- Zieger, B., Opher, M., Tóth, G., Decker, R. B., & Richardson, J. D. 2015, *JGR*, **120**, 7130